



The Murchison Greenstone Belt, South Africa: Accreted slivers with contrasting metamorphic conditions

Sylvain Block, Jean-François Moyen, Armin Zeh, Marc Pujol, Justine Jaguin, Jean-Louis Paquette

► To cite this version:

Sylvain Block, Jean-François Moyen, Armin Zeh, Marc Pujol, Justine Jaguin, et al.. The Murchison Greenstone Belt, South Africa: Accreted slivers with contrasting metamorphic conditions. *Precambrian Research*, Elsevier, 2013, 227 (April 2013), pp.77-98. <10.1016/j.precamres.2012.03.005>. <hal-00691575>

HAL Id: hal-00691575

<https://hal.archives-ouvertes.fr/hal-00691575>

Submitted on 11 May 2012

HAL is a multi-disciplinary open access archive for the deposit and dissemination of scientific research documents, whether they are published or not. The documents may come from teaching and research institutions in France or abroad, or from public or private research centers.

L'archive ouverte pluridisciplinaire **HAL**, est destinée au dépôt et à la diffusion de documents scientifiques de niveau recherche, publiés ou non, émanant des établissements d'enseignement et de recherche français ou étrangers, des laboratoires publics ou privés.

THE MURCHISON GREENSTONE BELT, SOUTH AFRICA: ACCRETED SLIVERS WITH CONTRASTING METAMORPHIC CONDITIONS

Sylvain Block^{a,b}

Jean-François Moyen^{a,b}

Armin Zeh^c

Marc Poujol^d

Justine Jaguin^d

Jean-Louis Paquette^a

a *Laboratoire Magmas et Volcans, UMR 6524 CNRS. Université Blaise Pascal, Rue Kessler, 63038 Clermont-Ferrand, France.*

b *Université Jean Monnet, 23 rue du Dr Paul Michelon, 42023 Saint-Étienne. France.*

c *Institut für Geowissenschaften, Altenhöfer Allee 1, D-60438 Frankfurt am Main, Germany.*

d *Géosciences Rennes, UMR CNRS 6118, Université de Rennes 1, Campus de Beaulieu, 35042 Rennes CEDEX, France.*

Corresponding author :

Sylvain Block

Université Jean Monnet, 23 rue du Dr Paul Michelon, 42023 Saint-Étienne. France.

Tel : +33(0)621333525

sylvain.block@gmail.com

Abstract

This paper presents new petrological and geochronological data for the ~3.09-2.92 Ga Murchison Greenstone Belt (MGB), located in South Africa's Kaapvaal Craton, and discusses their geotectonic implications. The MGB is made of three tectono-metamorphic units: the Silwana Amphibolites, the Murchison Unit and the La France Formation. They underwent contrasting clockwise pressure-temperature-deformation (P-T-D) histories, and are separated from each other by relatively narrow, high-strain shear zones, with a sinistral, transpressive top-to-the-south movement, consistent with the deformation patterns observed throughout the belt. These patterns are explained by a N-S compressional stress field, affecting the Murchison Belt between 2.97 and 2.92 Ga. Results of new petrological investigations indicate that ultramafic to felsic volcano-sedimentary rocks of the Murchison Unit underwent a greenschist- to lower-amphibolite-facies metamorphism at maximum P—T conditions of 5.6

hal-00691575, version 1 - 26 Apr 2012

40 ± 0.6 kbar at 570°C, along a relatively hot, minimum apparent geotherm of $\sim 30^\circ\text{C}/\text{km}$. In contrast, the
41 Silwana Amphibolites and the La France Formation were metamorphosed at much higher peak
42 metamorphic conditions of 8.7-10 kbar, 630-670°C, and 8-9 kbar, 600-650 °C respectively, and require a
43 colder apparent geotherm of $\sim 20^\circ\text{C}/\text{km}$. A retrograde, nearly isothermal-decompression P—T path
44 followed by isobaric cooling is also inferred for the La France Formation. The timing of the structural-
45 metamorphic overprint is bracketed between 2.97 and 2.90 Ga, which is constrained by U-Pb zircon ages
46 of a syn-deformation granite within the Murchison Unit and the post-deformation Maranda granite,
47 respectively. Monazite and xenotime from La France metapelites yield much younger ages of ca. 2.75 Ga,
48 with few inherited components at 2.92 Ga. They point to a later activation of the MGB, perhaps related
49 with tectono-thermal events in the Rooiwater Complex and the Pietersburg Greenstone Belt. The
50 relatively cold apparent geotherms recorded in the Silwana and La France rocks, the contrasted peak P—
51 T conditions between the different units, and the near isothermal decompression of the La France
52 Formation indicate that the Kaapvaal craton crust must have been cold enough to enable significant
53 crustal thickening and strain localisation along narrow shear zones and, as a consequence, fast tectonic
54 juxtaposition of rocks metamorphosed at different crustal depths. These features are similar to those
55 observed along Palaeozoic or modern day, oblique subduction-collision zones, but different to those of
56 hot Archaean provinces. We therefore interpret the MGB as representing part of an oblique collision-zone
57 between two terrains of the Kaapvaal craton: the Witwatersrand and Pietersburg terrains.

58
59 **Keywords :** Metamorphism, Archaean tectonics, Murchison Greenstone Belt, Kaapvaal craton.

60 61 62 **1. Introduction**

63
64 Many tectonic studies on various Archaean cratons have reported structural features in volcano-
65 sedimentary belts that differ from younger Proterozoic and Phanerozoic orogenic belts (e.g. Bouhallier et

66 al., 1993, 1995; Choukroune et al., 1995, 1997; Chardon et al., 1996, 1998, 1999). Linear fold and thrust
67 belts, strain localisation along crustal scale faults, juxtaposition of contrasted metamorphic domains
68 forming “paired metamorphic belts” (e.g., the Mesozoic Ryoke-Sanbagawa belts in Japan, Miyashiro,
69 1961; Brown, 2010 and references therein), tectonically driven exhumation processes, as well as features
70 that are typical of subduction, such as ophiolites, accretionary prisms and blueschist-facies to Ultra-High-
71 Pressure-facies metamorphism, are widely recognised in modern orogens. On the other hand, ubiquitous
72 craton scale shear zones, dome and basin strain patterns, deformation distribution on a regional scale, and
73 the relative homogeneity of erosion levels and metamorphic gradients are characteristic of many
74 Archaean granite-greenstone provinces (Binns et al., 1976; Park, 1992; Chardon et al., 2008, 2009). The
75 description of features in Archaean provinces interpreted to be related to subduction and modern-style
76 accretion tectonics has fed the debate on the onset of plate tectonics and on the evolution of tectonic
77 regimes through time (e.g. Komiya et al., 1999; Kusky et al., 2001; de Wit, 2004; Condie and Kröner,
78 2008; Cawood et al., 2009); and the recognition of contrasted tectono-metamorphic signatures between
79 modern and Archaean orogens led authors to invoke secular changes in the thermal regime of the Earth as
80 the factor driving the shift from one tectonic style to another (e.g. Komiya et al., 2002; Brown, 2007;
81 Gapais et al, 2009; Sizova et al., 2010). A wide range of models were proposed to account for the features
82 observed in Archaean provinces. An intellectual framework defined by two “end-member” models, with a
83 hot and weak lithosphere in the Archaean as opposed to a cold and strong lithosphere in the Proterozoic
84 and Phanerozoic eras has been widely adopted. However, given the wide variation in the rheological
85 properties of Phanerozoic lithospheres (Watts and Burov, 2003 and refs. therein), one can expect to be
86 confronted to such geographical disparities in Archaean cratons.

87 The heat budget of the lithosphere is a major control of its rheological properties, and as a consequence,
88 of the dominant tectonic regime in the crust. Metamorphic rocks record evidence of the pressure and
89 temperature evolution with time, which reflects the thermal environment under which the constituent
90 mineral assemblages equilibrated. Spatial distribution of peak P—T conditions provide information on the
91 spatial variation in thermal regimes; hence metamorphic studies are an important tool to investigate the

hal-00691575, version 1 - 26 Apr 2012

92 tectonic style of Archaean provinces. Although metamorphic studies, coupled with structural and
93 geochronological constraints, have contributed greatly to our understanding of modern orogenic processes
94 (e.g. Miyashiro, 1961; Ernst, 1973, 1975, 1988; Chopin, 1984; Smith, 1984; Brown, 2009),
95 metamorphism across Archaean granite–greenstone terrains has been comparatively under-studied.
96 Consequently, the lack of well-constrained metamorphic studies has hampered the development of a
97 geodynamic framework for the formation of granite–greenstone terrains. It has also led to the
98 generalisation in the literature of implicit assumptions on Archaean metamorphism, as some observations
99 relevant to specific Archaean provinces are taken to be a general rule.

100 Most granite–greenstone terrains are reported to have undergone metamorphism along high-Temperature,
101 low-Pressure apparent geothermal gradients. Metamorphic conditions are generally described as isobaric
102 across hundreds of kilometres, with isotherms parallel to the surface, or as grading progressively from
103 low-grade greenschist-facies to granulite-facies across kilometres-large and hundreds of kilometres-long
104 shear zones, where strain is distributed rather than localised (Grambling, 1986; Collins and Vernon, 1991;
105 Percival et al., 1992; Percival et al., 1994; Caby et al., 2000). Variations in metamorphic grade in Archaean
106 granite–greenstone terrains are frequently attributed to contact metamorphism linked to the emplacement
107 of granitoid bodies, or as the result of a “crustal overturn” (Van Kranendonk, 2002). However, an
108 increasing number of studies provide evidence for disparities in metamorphic patterns between Archaean
109 terrains. High P-low T metamorphism (18-20 kbar, 630°C) is reported from the Indian Bundelkhand
110 Craton at ca. 2.78 Ga (Saha et al., 2011); ca. 2.72 Ga eclogite-facies metamorphism is recorded in the
111 Belomorian belt of Russia (Volodichev, 2004; Brown, 2009; Mints et al., 2010). High metamorphic
112 gradients between terrains metamorphosed at different depths, and juxtaposed along planar tectonic
113 structures that localised deformation, are described in the Palaeoarchaean Barberton Greenstone Belt
114 (BGB), in the east of the Kaapvaal craton, South Africa (Kisters et al., 2003; Diener et al., 2005; Moyer,
115 2006) and in the Mesoarchaeon Point Lake orogen of the Slave Province, Canada (Kusky et al. 1991).

116 This study aims to unravel the tectono-thermal history of the northwestern part of the Archaean
117 Kaapvaal Craton in South Africa. In order to do so, the metamorphic conditions across the Murchison

Greenstone Belt, the nature of the contacts between the distinct tectono-metamorphic units, and the timing of the structural-metamorphic and magmatic processes were investigated. By coupling the different information, we intend to bring new insights into the geodynamic evolution that led to the formation of the MGB and to contribute to a broader understanding of Archaean tectonics.

2. Geological setting of the MGB

2.1. Regional context and geochronological constraints

The ENE-WSW trending Murchison Greenstone Belt is one of the volcano-sedimentary belts of the Archaean Kaapvaal craton of South Africa (Brandl et al., 2006; Robb et al., 2006) (Fig. 1). It is situated about 200 km north of the ca. 3.5-3.2 Ga Barberton Greenstone Belt (e.g. Kröner et al., 1991, 1992, 1996; Kamo and Davis, 1994; Dziggel et al., 2002), and about 80 km south of the 3.2-2.8 Ga Giyani Greenstone Belt (Kröner et al., 2000). It extends for ~140 km ENE-WSW, 15 – 20 km N-S, and is unconformably overlain by the Neoarchaeoan to Palaeoproterozoic sediments of the Transvaal Supergroup (Burger and Coertze, 1973; Altermann and Nelson, 1998) at its western extremity. Furthermore, it is located along the “Murchison-Thabazimbi Lineament” (Du Plessis, 1990), which is defined on the basis of geophysical data and interpreted to form an important terrain boundary in the northern Kaapvaal craton, separating the Witwatersrand terrain to the south from the Pietersburg terrain to the north (Good and de Wit, 1997; Anhaeusser, 2006; Zeh et al., 2009).

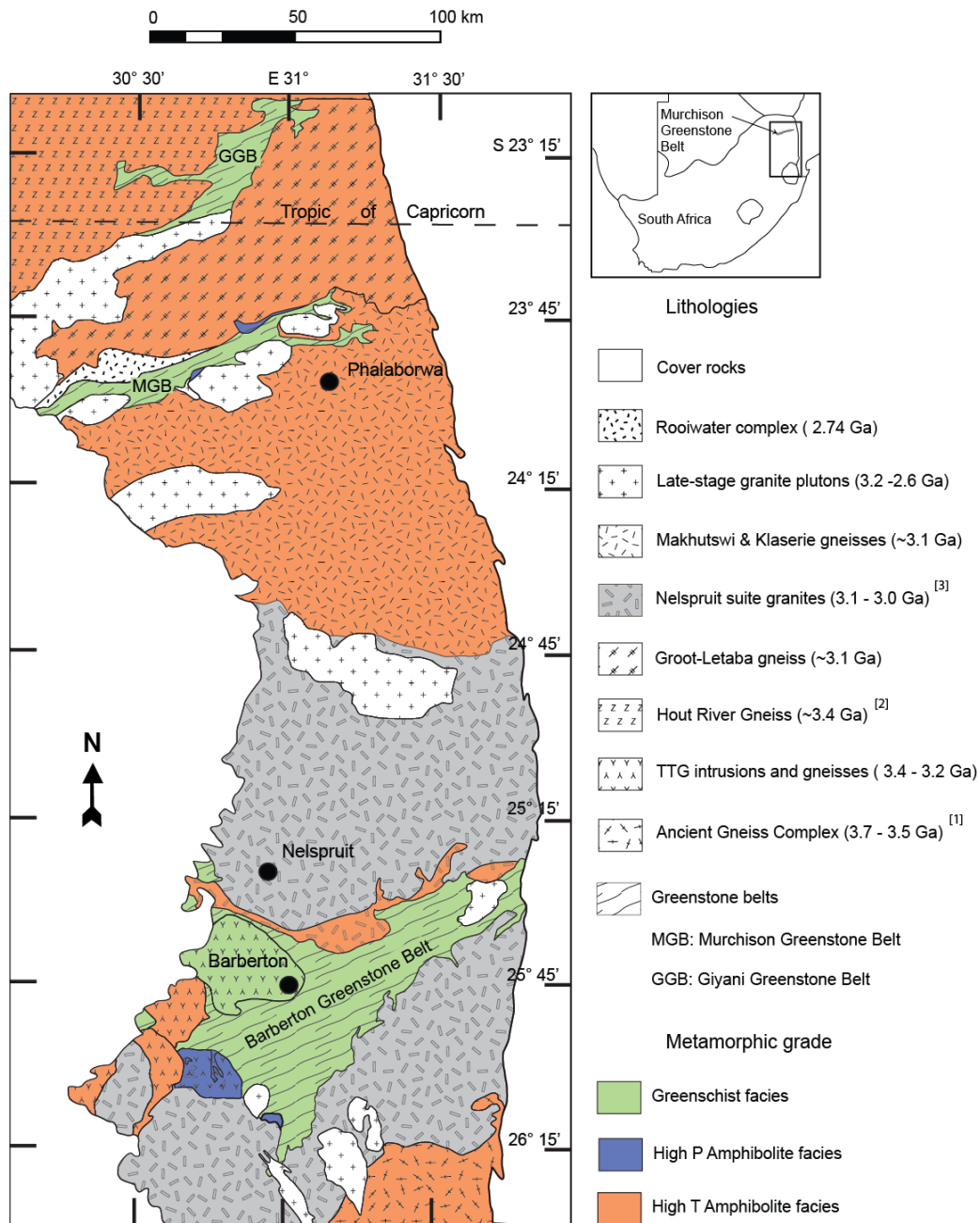


Figure 1:

Simplified geologic map of the north-eastern part of the Kaapvaal craton. Different colours represent domains with different metamorphic grades, inferred from sparse field observations and data from the literature. [1]: Kröner and Tegtmeier (1994); Compston and Kröner (1988), [2]: Kamo and Davis (1994), [3]: Brandl and Kröner (1993); Kröner et al. (2000). See text for other references.

At its northern margin, the supracrustal rocks of the MGB are bounded by the Rooiwater Complex and the Groot Letaba Gneisses. The Rooiwater Complex (Vearncombe et al., 1997) represents a mostly undeformed layered mafic intrusion emplaced at a minimum age of 2.74 Ga (Poujol et al. 1996) and

149 subsequently intruded by mafic dykes at 2.61 Ga (Zeh et al., 2009). Field evidence however suggest that
150 this age may correspond to a late resetting of geochronometers, and the emplacement age of the
151 Rooiwater complex is likely to be significantly older (Vearncombe, 1992). The contact between the
152 Rooiwater Complex and the MGB is tectonically reworked (Vearncombe, 1992). The Groot Letaba
153 Gneisses (Brandl and Kröner, 1993) comprise a series of locally migmatised dark-grey gneisses, tonalites
154 and trondjhemites. They were mostly emplaced at ca. 3180 – 3000 Ma, with the exception of some ca.
155 2885 ± 4 Ma discordant leucogneisses (Brandl and Kröner, 1993). The basement directly to the south of
156 the MGB is made of granitoids (TTGs) of the French Bob's Mine, emplaced 3228 ± 12 Ma ago (Poujol et
157 al. 1996); and by younger intrusive granitoids of ca. 3110 – 3060 Ma (Brandl and Kröner, 1993 ; Poujol
158 and Robb, 1999). The southern margin of the MGB was affected by the episodic intrusion of granite
159 plutons and pegmatites of the Voster Suite, at ca. 3020, 2970, 2900, 2820 and 2680 Ma, respectively for
160 the Baderoukwe, Discovery, Maranda, Willie, Mashishimale plutons, and associated intrusions (Fig. 2)
161 (Poujol et al 1996; Poujol and Robb, 1999; Poujol, 2001; Zeh et al., 2009). Published geochronological
162 data indicate that the supracrustal sequence of the MGB formed over a period of more than 100 Ma,
163 between ca. 3090 and 2970 Ma (Poujol et al., 1996, Poujol et al., 2001).

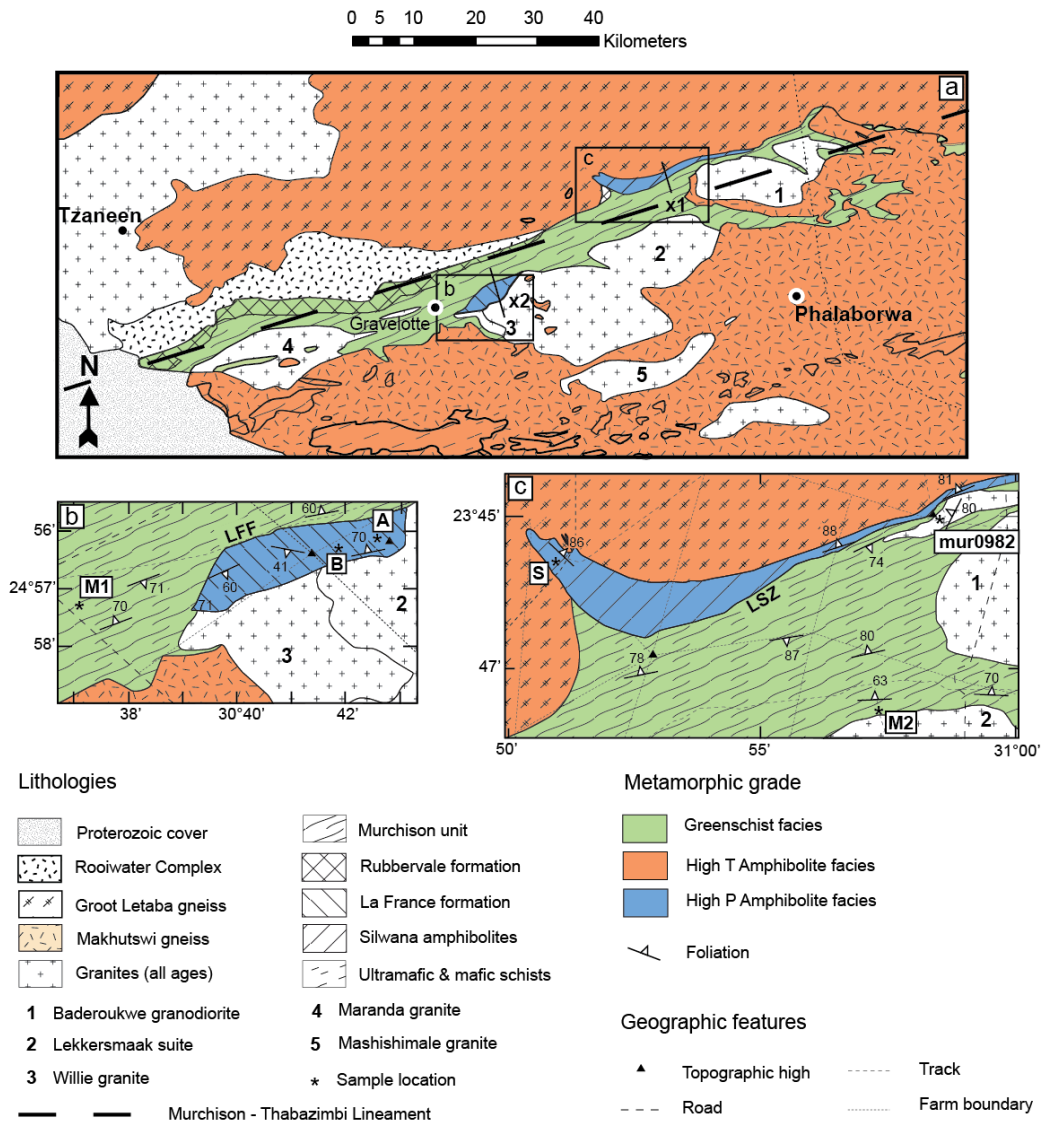


Figure 2:

(a) Simplified geologic and metamorphic map of the Murchison Greenstone Belt and its surroundings. (b, c) Detailed maps with the location of samples (A, B, S, M1, M2 and mur0982) discussed in the text, modified from Vearncombe et al. (1992). The lines marked with x_1 and x_2 correspond to the cross section shown in Fig. 9. LFF = La France Fault, LSZ = Letaba Shear Zone.

2.2. Structural-Metamorphic Units of the MGB

Based on structural and lithological criteria, Vearncombe et al. (1992) subdivided the MGB into four major, ENE-WSW-striking lithostratigraphic domains (Fig. 2):

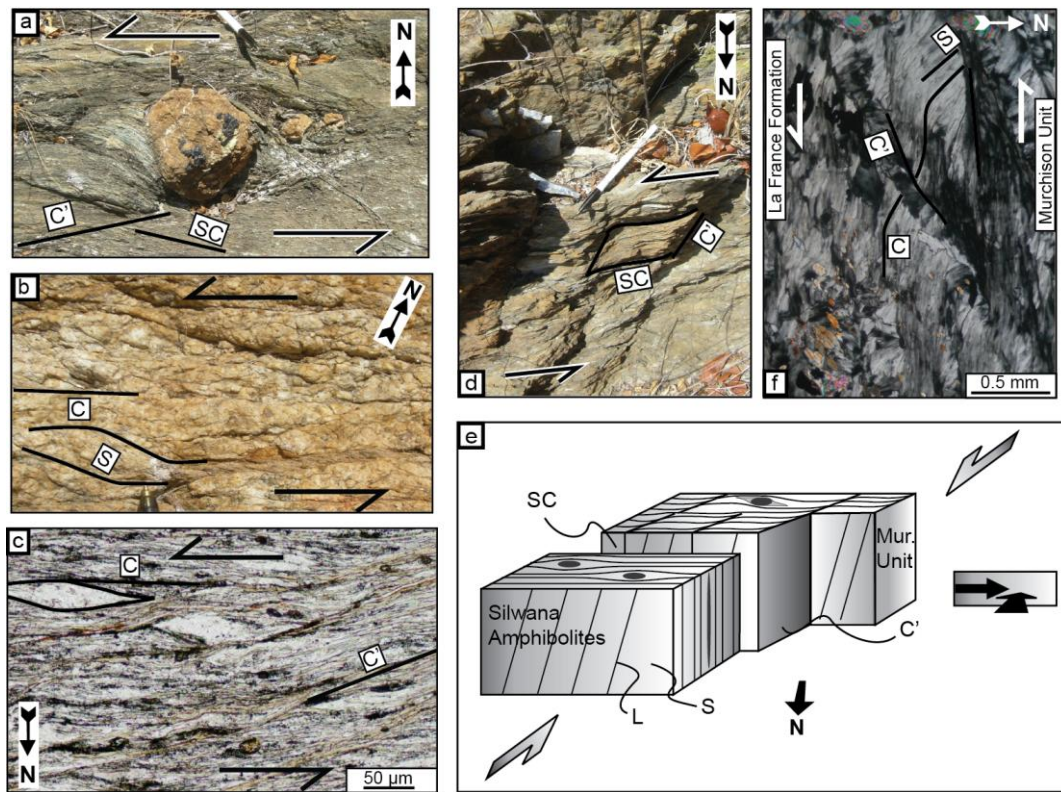


Figure 3:

Fabrics at or near to the sheared contacts between the different terrains of the MGB. (a). Asymmetric pressure shadow zones around a carbonate nodule in a mylonitic carbonates of the Murchison Unit, in the Letaba Shear Zone. (b) S – C fabrics in a deformed granite within the Letaba Shear Zone. (c) Microstructures observed in the quartz-chlorite schists of the Letaba Shear Zone include C' shear bands and mineral fish. (d) S-C - C' planes in quartz-chlorite schists of the Murchison Unit, in the Letaba Shear Zone. The kinematic indicators in (a), (b), (c) and (d) provide evidence for sinistral motion along the shear zone. (e) Synopsis of the structures observed along the Letaba shear zone. The flattening fabric in the Silwana amphibolites, that formed under upper- amphibolite facies conditions, occurs in close contact with mylonitised schists of the Murchison Unit, which provide evidence for a sinistral strike-slip under greenschist facies conditions. The latter is interpreted to have occurred in a transpressive setting and was accompanied by a top-to-the-south motion. (f) S – C – C' fabrics in a chlorite schists of the Murchison Unit, near the contact with the La France Formation, provide evidence for top-to-the-south motion. The C planes are subvertical.

The largest lithological domain of the MGB, hereafter referred to as the “**Murchison Unit**”, includes the MacKop, Weigel, Leydsdorp and Mulati formations of the South African Committee for Stratigraphy (SACS) (1980) nomenclature. It consists of mafic and ultramafic volcanic rocks along with volcano-

195 sedimentary and sedimentary rocks. The most representative lithologies of the domain are mafic quartz-
196 chlorite and albite-chlorite-actinolite schists, locally pillowed. The volcano-sedimentary rocks are locally
197 interbedded with BIFs and with aluminous quartzites and conglomerates. The clastic sediments form
198 prominent ridges, often corresponding to synform limbs in the central part of the MGB. Massive
199 carbonates and carbonate schists crop out mostly along a high-strain shear zone in the centre of the belt,
200 flanked by quartzite ridges to the north: the Antimony Line (Viljoen et al., 1978; Vearncombe, 1988a,
201 1992), which hosts Sb (\pm Au) mineralisation. Serpentinite lenses occur in the southern part of the belt.
202 Stratigraphic relationships within this unit remain unclear, as contacts between formations are tectonic in
203 nature (Vearncombe, 1992). U-Pb zircon ages provide evidence that the Weigel Formation volcanics were
204 emplaced at ca. 3.09 Ga, while a maximum age of deposition for the MacKop conglomerate was found to
205 be ca. 3.08 Ga old (Poujol et al., 1996).

207 The **Rubbervale Formation** is exposed along the northwestern flank of the MGB. It comprises quartz-
208 porphyroclastic schists, along with felsic lavas, tuffs and breccias. This formation also hosts the major
209 VMS-type deposit of the so-called ‘Cu-Zn’ line (Schwarz-Schampera et al., 2010). Emplacement of the
210 Rubbervale formation was dated at ca. 2.97 Ga (Brandl et al. 1996 ; Poujol et al. 1996 ; Poujol 2001).

211 The third unit, the **Silwana Amphibolites** (Vearncombe et al., 1992; part of the Rubbervale formation in
212 the SACS terminology), is exposed in the north-eastern part of the MGB, and represent a 0.1-1.5 km wide
213 sliver of amphibolites, rarely garnet-bearing, displaying a centimetric layering.

214 **La France Formation** (Vearncombe et al., 1992, SACS terminology) mostly consists of quartzite and
215 kyanite- staurolite- garnet-bearing biotite micaschists.

216
217 Vearncombe et al. (1988b) and Vearncombe (1992) stated that the Silwana Amphibolites and the rocks of
218 the La France Formations experienced a higher degree of metamorphism than the rocks of the Murchison
219 Unit and Rubbervale Formation, which together form the core of the MGB (Fig. 2). Metamorphic P—T
220 conditions were estimated to be > 5kbar, 550-650°C for the La France Formation, while field

221 observations qualitatively suggested a higher grade metamorphic conditions in the Silwana Amphibolites
 222 compared to the Murchison Unit.

223

224 *Table 1:*

225 *Summary of the mineral assemblages and textures developed in the different formations of the MGB.*

226

Terrain	Rock type	Outcrop occurrence	Mineral assemblages	Texture	Sample
La France Formation	Gt- St-bearing micaschist	Bt-schist with thin metamorphic banding, crenulated. Protruding elongated Gt and St	Peak (syn-D ₂): Gt + St + Bt + Ms + Q Post-peak: Bt, Hem	Large Gt and St porphyroblasts, thin Bt beds, crenulated.	A
La France Formation	Ky (± St)-bearing micaschist	Bt-schist with thin metamorphic banding. Protruding elongated Ky.	Peak (syn-D ₂): Ky + Bt + Ms + Pl ± St ± Ilm ± Ru + Q Retrograde: Bt + Sill + Pl + Crd / Bt + Chl + Ms + St ± Ky Accessory : Mnz, Xno	Large Ky porphyroblasts, elongated parallel to Bt beds. Retrograde Crd, Bt - Chl - Ms simplectite, St	B
Murchison Unit	Act-bearing metabasite	Green metabasite, no pervasive tectonic fabric	Peak : Act + Ab + Chl + Ep + Sph	Garbenscheifer texture : needle-shaped Act, Chl in late shear bands	M1
Murchison Unit	Aluminous quartzite	Fine grained quartzite with well developed metamorphic cleavage, parallel to micaceous bedding	Peak : Gt + Bt + Ms + Q Retrograde: Chl	Thin aligned Ms and Bt beds with small Gt, intercalated with protogranular quartz beds	M2
Silwana Amphibolites	Gt- Hbl-bearing amphibolite	Dark, fine grained, massive « amphibolitic gneiss » with occasional garnet-bearing layers.	Peak: Hbl + Pl + Gt + Bt + Ilm + Q Retrograde: Chl, Ep Accessory: Ap, Calc	Equigranular texture with aligned Hbl. Intercalation of Hbl and recrystallised Pl and quartz beds. Gt porphyroblasts with Ilm and Hbl inclusions	S

227
228

229 **2.3. Contact zones between the units of the MGB**

230

231 The different units of the MGB are separated from each other by large-scale ductile shear zones. A
 232 detailed structural study of the MGB is beyond the scope of this paper and only a brief review of the
 233 nature of the contacts is presented here. A description of the regional strain field and the tectonics of the
 234 MGB are given in Vearncombe (1988b); Kusky and Vearncombe (1997) and Jaguin et al. (2012).

235

236 **2.3.1. The Letaba Shear Zone**

10.100691575, version 1 - 26 Apr 2012

237
238
239
240
241
242
243
244
245
246
247
248
249
250
251
252
253
254
255
256
257
258
259
260
261
262

To the north-east of the MGB, the Letaba Shear Zone (LSZ) separates the Silwana Amphibolites from low-grade, quartz-chlorite and carbonate schists of the Murchison Unit. The contact is very sharp and shows signs of a tectonic melange. The Silwana Amphibolites display a penetrative flattening fabric formed under amphibolite-facies conditions. The cleavage is subvertical and bears a steep (pitch $>75^\circ$) easterly plunging mineral elongation lineation. Asymmetric shear sense indicators are rare within this formation: pressure shadow zones around garnet porphyroblasts are symmetrical, and no shear bands were observed in thin sections. Towards the contact with the Silwana Amphibolites, the Murchison Unit schists display a mylonitic microstructure and a significant grain size reduction. The mylonites exhibit an NE-SW cleavage, parallel to the contact between the two formations. The cleavage has a moderate to sub-vertical dip to the south and carries a mineral elongation lineation dipping moderately (pitch $> 40^\circ$) to the east. Asymmetric shear sense indicators, such as pressure shadow zones around primary carbonate nodules consistently point to a sinistral shear (Fig. 3a). The same shear direction is also reflected by SC-C'-fabrics and extensional crenulation cleavages (Berthé et al., 1979; Platt and Vissers, 1980), indicative of stretching parallel to the foliation, which are well developed within the mylonitised quartz-chlorite-schists (Fig. 3c, d). At the “Witkop” locality (near sample mur0982 in Fig. 2), where the relationships between the different units are clearly exposed, a deformed granite intrudes the greenschist-facies mylonites of the Murchison Unit. No contact metamorphism was observed in the quartz-chlorite schists around the granite body. The granite displays well-expressed C-S structures (Fig. 3b). S and C surfaces have a shallow to sub-vertical dip towards the NW, and C surfaces carry a mineral elongation lineation that plunges to the NE. The deformation patterns provide evidence for a sinistral, transpressive setting with a top-to-the-south directed motion (Fig. 3e). The strike-slip component of the finite deformation that is well expressed in the greenschist facies mylonites of the Murchison Unit is not observed in the Silwana Amphibolites.

2.3.2. The “La France Fault”

The La France Formation is separated from the greenschist-facies rocks of the Murchison Unit by a highly deformed zone a few dozen metres wide, hereafter named the “La France Fault”. The lithologies in contact with the northern boundary of the La France Formation range from talc schists and serpentinites to chlorite schists containing primary carbonates. Within the shear zone, the schists display open to tight folds with decimetric wavelengths. At least two sets of such folds are found, with axes displaying shallow plunges of 5 - 10° to the NW and SW respectively. Unfortunately, poor outcrop conditions restricted to exploration trenches, among other constraints, prevented a more extensive study of fold patterns. Mineral elongation lineations on shear-zone-parallel cleavages plunge preferentially to the NE, whereas shear sense indicators, such as mineral fish and asymmetric shadow zones around porphyroblasts, point to a top-to-the-south motion (Fig. 3f). These patterns in combination provide evidence for a sinistral component during a general top-to-the-south reverse faulting, similar to that observed along the Letaba Shear Zone. The latter interpretation is also in agreement with structures observed within the La France formation to the south of the shear zone. The La France schists exhibit recumbent folds axial planar to the metamorphic banding, and are affected by crenulations with shallow-plunging axes. These structures are illustrative of a shortening accommodated by reverse faulting.

To the south, the La France Formation is in contact with the 2795 ± 8 Ma Ma Lekkersmaak granite (Zeh et al. 2009) and with the 2820 ± 38 Ma Willie granite (Poujol, 2001), which form part of the Voster Suite. The granites contain micaschist xenoliths derived from the La France Formation. They are mostly undeformed except for occasional shear bands formed under sub-solidus conditions. The field relationships clearly indicate that the Lekkersmaak and Willie intrusions postdate the deformation and metamorphism in the La France Formation.

2.3.3. Other structures

289 The Antimony Line is a steeply north dipping mineralised shear zone within the Murchison Unit. The
290 dominant fabric consists of isoclinal folds axial-planar to the metamorphic banding, along with S-C
291 planes indicating a top-to-the-south motion. Mineral elongation lineations plunge vertically to moderately
292 eastwards. These structures illustrate a general transpressive, sinistral setting in the Murchison Unit,
293 accompanied by a significant reverse component (Vearncombe et al., 1988, 1992). They are consistent
294 with the kinematics observed in the Letaba and La France shear zones. At a larger scale, they are in
295 general agreement with the regional-scale sinistral transpressive regime and illustrate deformation
296 localisation in the regional strain field, described in Jaguin et al. (2012).

298 299 **3. Petrography, fabrics and mineral chemistry**

300
301 A summary of the main petrographic and textural characteristics of the rocks sampled from the different
302 formations of the MGB is presented in Table 1. Details of analytical techniques used to determine mineral
303 chemistry are given in Appendix (A1).

304 305 **3.1. La France Formation**

306
307 Field observations and microstructural studies of quartzites and micaschists of the La France Formation
308 provide evidence that a primary compositional layering S_0 was modified during an early D_1 deformation
309 event, leading to the formation of a composite S_0/S_1 foliation. The S_0/S_1 foliation was subsequently
310 affected by the main D_2 deformation event (Fig 4b, e). The latter caused the formation of the predominant
311 S_2 fabric that is axial-planar to recumbent folds. The S_2 planes are mostly defined by quartz (Q) ribbons,
312 biotite (Bt), and minor muscovite (Ms). They bear a L_2 mineral elongation lineation. In metapelitic layers
313 syn-deformation staurolite (St), garnet (Gt) and kyanite (Ky) porphyroblasts can additionally be observed,
314 although the latter two are not found together in the same sample (Fig. 4a and 4c). Plagioclase feldspar

(Pl) sillimanite (Sill) and cordierite (Crd) occasionally occur in the kyanite-bearing schists. The S_2 schistose planes were crenulated as a result of a D_3 deformation event, leading to the formation of kinks with a mm- to cm-scale wavelength, and of a crude S_3 cleavage. In kyanite-bearing micaschist, some kyanite, staurolite and chlorite were kinked during D_3 crenulation, while new chlorite, staurolite and muscovite develop in the kink axes (Fig. 4f). The final minerals thus form syn- to post- D_3 assemblages.

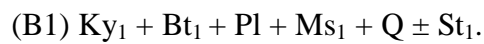
The garnet-bearing micaschists display the following peak assemblage:

(A): Gt + St + Bt₁ + Ms₁ + Q

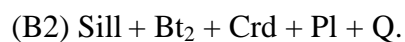
In these rocks, syn-deformation garnet porphyroblasts with quartz inclusion trails are commonly overgrown by syn-deformation staurolite, with similarly oriented quartz inclusion trails, indicating the successive formation of both minerals during the deformation event D_2 (Fig. 4d). Hematite is always a retrograde phase, which formed along cracks in altered garnet grains, mostly at garnet rims. The peak metamorphic fabric is overgrown by post-deformation biotite (Bt₂) and muscovite (Ms₂). Garnet porphyroblasts show a continuous prograde growth zoning, characterised by increasing X_{Py} ($Mg/(Mg+Fe+Ca+Mn)$) from 0.05 to 0.09 and Mg# ($Mg/(Fe+Mg)$) from 0.07 to 0.09, and decreasing X_{Sps} ($Mn/(Mg+Fe+Ca+Mn)$) from 0.12-0.06 to 0.03 and X_{Grs} ($Ca/(Mg+Fe+Ca+Mn)$) from 0.07 to 0.06, all from core to rim. Staurolite has Mg# of 0.12-0.14. The Mg# of syn- D_2 biotite (Bt₁) ranges from 0.32 to 0.44 range, while post- D_2 biotite (Bt₂) has Mg# = 0.44, suggesting partial reequilibration of Bt₁. Muscovite (Ms₁ and Ms₂) has low Si of 3.05 a.p.f.u. (atoms per formula unit) and a relatively high paragonite component, as is reflected by $Na/(Na+K+Ca) = 0.17$. Representative mineral compositions are shown in Table 2.

Kyanite-bearing schists (B) provide evidence for the successive formation of different equilibrium assemblages during peak and retrograde evolution. The peak metamorphic conditions are illustrated by

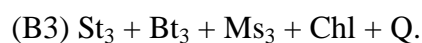
341 syn-D₂ kyanite porphyroblasts that commonly contain biotite, muscovite and quartz inclusions. Some
342 rocks additionally bear syn-D₂ staurolite porphyroblasts, produced with kyanite, presumably during the
343 progressive breakdown of chlorite (which completely reacted out). Thus the thin section observations
344 indicate that the following assemblage formed during D₂ deformation at peak pressures (Fig. 4b):
345



347
348 The occurrence of prismatic sillimanite, as well as of fibrolite around kyanite indicates that the kyanite-
349 bearing schists crossed the phase transition $Ky \rightarrow Sill$. The coexistence of sillimanite and cordierite
350 (Crd) (Mg# = 0.75-0.77; Na= 0.11 a.p.f.u.), which together form patches about 0.5mm wide, shows
351 furthermore that assemblage (B1) was later (partially) replaced by the assemblage:



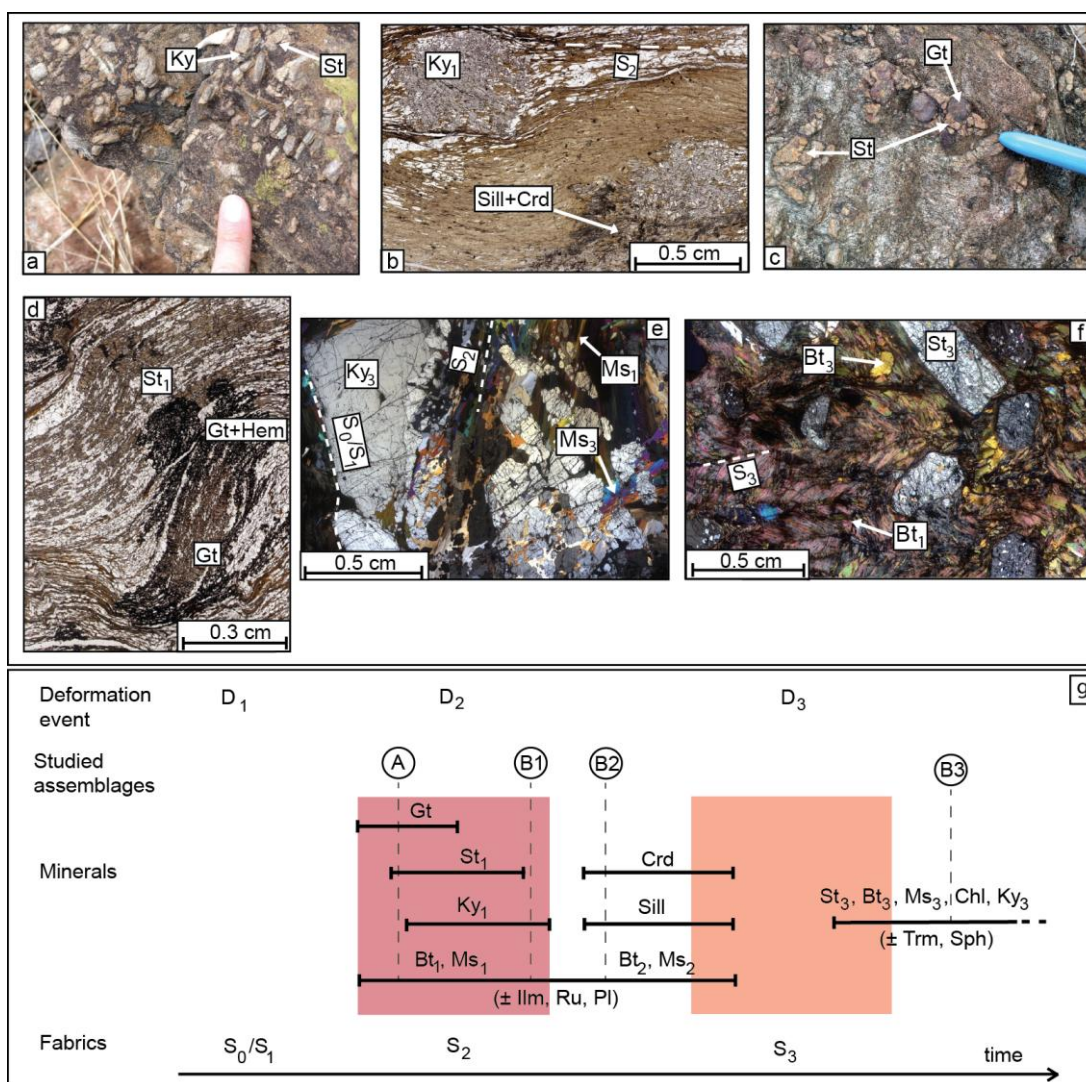
354
355 Subsequently, the cordierite grains were partially replaced by a new generation of micrometric staurolite
356 grains, which are closely intergrown with fine grained, chlorite and symplectitic muscovite. These
357 intergrowth relationships indicate that the final mineral assemblage in the kyanite-bearing schists was:
358



360
361 Retrograde staurolite St_3 generally has higher Mg# of 0.19-0.24 than the prograde and peak metamorphic
362 staurolite St_1 , with Mg# of 0.13-0.20. In contrast, biotite from all the successive assemblages (Bt_1 to Bt_3)
363 overlap in compositions, with Mg# = 0.62-0.64, $Ti^{vi} = \sim 0.06$. This is interpreted to be the result of
364 widespread chemical reequilibration of biotite composition during metamorphic evolution. Prograde
365 muscovite (Ms_1) always shows lower Na/(Na+K+Ca) of 0.08 and higher silica contents (Si = 3.15
366 a.p.f.u.) than retrograde muscovite (Ms_3), with Na/(Na+K+Ca) = 0.18 and Si= 3.02 a.p.f.u.. M.

367 $/(Na+K+Ca) = 0.08$. Retrograde chlorite of assemblage (B3) has $Mg\# = 0.66-0.69$, and high-Al contents
 368 of 1.35 a.p.f.u. Plagioclase grains show a wide range of chemical compositions, with $X_{An} (Ca/Ca+Na) =$
 369 0.09 to 0.41, and a majority of grains having $X_{An} \sim 0.4$.

370 In one sample from the same formation, centimetric euhedral kyanite (Ky_3) and staurolite (St_3) crystals
 371 overgrow the S_2 metamorphic banding, together with millimetric biotite and muscovite grains (Fig. 4e
 372 and 4f). This assemblage, equivalent to (B₃) in more aluminous lithologies, suggests that the $Sill \rightarrow Ky$
 373 phase transition was crossed during the retrograde evolution of the rock. Furthermore, the retrograde
 374 assemblages (B₂) and (B₃) are characterised by the formation of abundant hydrated minerals, indicating a
 375 secondary, H_2O -rich fluid enrichment after peak metamorphism.



376
 377 **Figure 4:**
 378 *Petrographic features observed in rocks of the La France formation. (a) Biotite micaschist with*
 379 *protruding staurolite (St) and kyanite (Ky) porphyroblasts. (b) Thin section of a kyanite- staurolite-*

380 cordierite-bearing micaschist (sample B). Ky porphyroblasts are surrounded by foliation-parallel biotite
381 and quartz (top), or are overgrown by patches of sillimanite and cordierite. (c) Garnet (Gt)- staurolite-
382 bearing micaschist (sample A). (d) Thin section of sample A showing highly deformed and rotated St and
383 Gt porphyroblasts (syn-D₂), set in a matrix of biotite, muscovite and quartz. Hematite (Hem) occurs along
384 cracks mostly in garnet rims, probably resulting from retrograde alteration. Biotite and muscovite define
385 the syn-D₂ metamorphic banding. (e) and (f) Thin sections of a Ky- St-bearing schist from the La France
386 formation showing, (e) a compositional layering S₀/S₁ delimiting a kyanite and muscovite-rich layer, with
387 Ky overgrowing the D₂ metamorphic fabric, (f) a crenulated domain, with euhedral staurolite and a crude
388 S₃ cleavage. (g) Synopsis showing the relative temporal relationships between deformation and
389 assemblage formation in the La France Formation (Ilm: Ilmenite, Ru : Rutile, Trm : Tourmaline, Sph :
390 Sphene).
391

392 3.2. Silwana Amphibolites

393
394 The Silwana Amphibolites trend ENE – WSW and show a vertical to steeply north-dipping S₀/S₁ layering
395 defined by modal variations of quartz, plagioclase and hornblende (Hbl) across bands about 10 cm thick.
396 On a smaller scale, the amphibolites develop a planar (S > L), flattening tectonic fabric S₂. The
397 metamorphic banding S₂, is subparallel to the S₀/S₁ layering. It is defined by the alternation of millimetric
398 hornblende-rich and quartz- plagioclase-rich bands. The latter display an equigranular texture, suggesting
399 a relatively high temperature recrystallisation (>500°C). The S₂ foliation bears a dominant steep easterly
400 dipping mineral lineation L₂ defined by hornblende. At the north-western extremity of the sliver, the
401 strike of the layering changes dramatically from ENE-WSW to NW–SE, with a steep north-easterly dip,
402 while the S₂ foliation carries a steep, north-plunging mineral elongation lineation. It is likely that both the
403 ENE- and NW-trending structures (and related lineations) result from activation of a conjugate shear
404 system. Garnet occurs as an additional phase in rare Al- and Fe-rich layers. Biotite is also present in small
405 proportions (~1-2 modal %). Epidote (Ep) is a retrograde phase and frequently formed in cross-cutting
406 veins, in association with carbonates. Chlorite is found in cracks within garnet porphyroblasts The peak
407 metamorphic assemblage is interpreted to be:
408

409 (S) Gt + Hbl + Pl + Bt + Ilm + Q.

410
411 The garnet porphyroblasts show a slight prograde growth zoning, as is reflected by increasing X_{Py} (from
412 0.055 to 0.060, Mg# varies from 0.67 to 0.73) and X_{Grs} (from 0.13 to 0.15), and decreasing X_{Sps} (from
413 0.04 to 0.03) and X_{Alm} ($Fe/(Fe+Mg+Ca+Mn)$ from 0.77 to 0.76) from core to rim. Garnet contains
414 inclusions of hornblende, quartz and ilmenite. Hornblende inclusions in garnet show some scatter in their
415 chemical composition, with Mg# = 0.21–0.26 and Ca/Na = 3.0-3.6, compared to Mg# = 0.23-0.26 and
416 Ca/Na = 2.8-3.0 for matrix hornblende. Matrix plagioclase has a constant chemical composition, with X_{An}
417 = 0.17. Biotite occurrence is limited, with small grains elongated parallel to hornblende, and some
418 randomly oriented grains occurring around garnet. All matrix biotites show similar compositions with
419 Mg# = 0.22-0.26 and $Ti^{vi} = 0.1$ a.p.f.u.. Retrograde chlorite (Mg# = ~0.36) only formed along cracks in
420 the garnet porphyroblasts.

421 422 423 **3.3. Murchison Unit**

424
425 Strain distribution in the Murchison Unit is fairly heterogeneous. Minor domains, far from tectonic
426 discontinuities, are almost undeformed, but most rocks displays a pervasive schistose fabric and provide
427 evidence for a poly-phased deformation (Vearncombe, 1988 ; Vearncombe et al., 1988, 1992 ; Jaguin et
428 al., 2012). Primary sedimentary structures S_0 , are only preserved in competent layers. Stratigraphic
429 contacts between the different formations of the Murchison Unit have been completely reworked by
430 tectonic processes during the successive deformation events. A first deformation episode D_1 corresponds
431 to the formation isoclinal folds axial-planar to a S_1 cleavage trending ENE. These isoclinal folds are
432 transposed by E-W trending, S-shaped asymmetric folds, axial planar to a S_2 cleavage, formed during a
433 second deformation event, D_2 . However, it is generally difficult to attribute the pervasive cleavages to
434 either D_1 or D_2 . None of our samples exhibit the D_3 crenulation cleavage, which was recognised by

435 Vearncombe et al. (1988, 1992) in rocks near to the Antimony Line. For P—T path estimates, we
436 investigated a sample from a nearly undeformed metamafic rock from the centre of the Murchison Unit,
437 south of the Antimony Line (sample M1); and a sample from a deformed quartzite with metapelitic layers
438 from the southern edge of the Murchison Unit (sample M2), a few dozen metres north from the contact
439 with the Makhutswi gneisses (Fig. 2). The metabasite sample M1 contains the following peak
440 metamorphic mineral assemblage:

441
442 (M1) Act (actinolite) + Ab (albite) + Ep + Chl + Sph (sphene)

443
444 with Chl mostly in late shear bands. The actinolite needles display a garbenscheifer texture, which might
445 represent pseudomorphs of primary magmatic textures, and have Mg# = 0.67-0.72. The feldspar is pure
446 albite ($X_{An} \leq 0.01$). Chlorite has Mg# = 0.55-0.56 and $Al^{vi} = 1.20$ a.p.f.u..

447
448 The metapelitic-quartzitic sample M2 displays the following peak mineral assemblage:

449
450 (M2) Gt + Ms + Bt + Chl + Qtz,

451
452 and additionally contains retrograde chlorite along garnet cracks. Garnet porphyroblasts have diameters <
453 0.5mm and do not display any chemical zoning. The garnets have a high almandine components of X_{Alm}
454 = 0.8, low pyrope and spessartine components ($X_{Py} = X_{Sps} = \sim 0.1$), and Mg# = 0.08-0.10. Biotite is Ti-
455 poor ($Ti^{vi} = 0.07$ a.p.f.u.) and has a Mg# = 0.39-0.44. Chlorite has Mg# = 0.36-0.39 and $Al^{vi} = 1.55-1.70$
456 a.p.f.u. Muscovite is Na-poor, with $Na/(Na+K+Ca) = 0.13$, and Si = 3.1 a.p.f.u..

457
458 *Table 2:*

459 *Major element compositions and structural formulae of representative mineral analyses of the peak and*
460 *retrograde assemblages in lithologies from the La France Formation, Murchison Unit and Silwana*
461 *Amphibolites.*

Sample	A (garnet- staurolite micaschist of the La France Formation)										
Mineral phase	Gt (core)		Gt(rim)	St (core)		St (rim)	Bt ₁	Bt ₁	Bt ₂	Ms ₁	Ms ₂
wt%											
Na ₂ O				b.d.l.	b.d.l.	0.08	0.16	0.22	1.23	1.31	
MgO	1.36	1.67	2.21	1.36	1.22	7.39	5.10	8.19	0.42	0.45	
Al ₂ O ₃	20.7	20.7	21.0	53.9	54.2	21.6	21.3	19.8	36.6	36.5	
SiO ₂	36.5	36.7	36.6	26.4	26.3	37.9	36.4	34.8	46.0	45.9	
K ₂ O						7.22	7.50	6.61	9.22	9.46	
CaO	2.65	2.07	1.95	b.d.l.	b.d.l.	0.14	0.16	0.08	0.01	0.04	
TiO ₂				0.22	0.34	0.98	0.65	0.95	0.09	0.07	
Cr ₂ O ₃						0.03	0.05	0.03	0.07	0.01	
MnO	5.44	3.59	1.17	0.02	0.06	0.01	b.d.l.	b.d.l.	b.d.l.	0.01	
FeO	34.2	35.0	37.6	15.7	15.1	16.8	19.4	18.4	1.16	1.04	
Total	100.8	100.4	100.4	97.6	97.2	92.1	90.7	89.1	94.8	94.7	
Oxygens	12	12	12	48	48	22	22	22	22	22	
Si	5.93	5.97	5.93	7.42	7.41	5.76	5.73	5.54	6.11	6.11	
Al ^{IV}	0.07	0.03	0.07	0.58	0.59	2.24	2.27	2.46	1.89	1.89	
Al ^{VI}	3.94	3.98	3.90	17.3	17.4	1.70	1.59	1.26	3.84	3.83	
Fe ³⁺	0.19	0.03	0.25	0.67	0.55						
Ti				0.05	0.07	0.10	0.11	0.11	0.01	0.01	
Cr						0.00	0.00	0.00			
Mg	0.53	0.39	0.33	0.57	0.51	1.58	1.67	1.94	0.08	0.09	
Fe ²⁺	4.90	4.87	4.39	3.03	3.00	2.10	2.12	2.45	0.13	0.12	
Mn ²⁺	0.16	0.37	0.75	0.01	0.01	0.00					
Ca	0.34	0.39	0.46			0.07	0.02	0.01	0.00	0.01	
Na						0.01	0.02	0.07	0.32	0.34	
K						1.23	1.39	1.34	1.56	1.61	
x[Py]	0.05	0.06	0.09								
x[Alm]	0.75	0.81	0.83								
x[Sps]	0.12	0.06	0.03								
x[Grs]	0.07	0.06	0.06								
Fe[fcel]									0.06	0.06	
Mg[mcel]									0.04	0.04	
Al[mphen]									0.89	0.90	

00691575, version 1 - 26 Apr 2012
 462

Sample	B (kyanite- plagioclase micaschist of the La France Formation)											
Mineral phase	Pl	Pl	St ₃	St ₃	Bt ₁	Bt ₃	Crd	Crd	Wm ₁	Wm ₃	Chl	Chl
wt%												
Na ₂ O	6.65	10.5			0.35	0.21	0.68	0.44	0.36	1.41	b.d.l.	0.03
MgO	0.01	0.02	1.98	2.17	13.26	14.40	9.56	9.68	2.76	1.19	18.8	19.4
Al ₂ O ₃	26.9	21.2	54.1	53.9	19.4	19.2	32.6	32.8	33.1	36.8	22.9	22.7
SiO ₂	57.3	66.1	28.9	29.1	36.5	35.2	49.1	49.0	46.6	46.0	25.5	26.0
K ₂ O	0.04	b.d.l.			9.12	8.40	0.01	0.02	6.02	9.28	0.44	0.68
CaO	8.45	1.99	b.d.l.	b.d.l.	0.04	0.04	0.07	0.03	0.42	0.02	0.10	0.05
TiO ₂	0.01	b.d.l.	0.13	0.05	1.09	0.69	0.06	b.d.l.	0.00	0.04	0.02	0.05
Cr ₂ O ₃			0.06	b.d.l.	0.24	0.14					0.05	0.37
MnO	0.01	0.02	0.48	0.42	0.08	0.13	0.19	0.12	0.01	0.02	0.16	0.11
FeO			12.3	12.2	13.9	15.3	5.57	5.41	2.79	1.06	17.3	16.4

hal-00691575, version 1 - 26 Apr 2013

Fe ₂ O ₃	b.d.l.	0.06										
Total	99.4	99.8	98.0	97.8	94.0	93.7	97.9	97.4	92.0	95.9	85.2	85.8
Oxygens	32	32	48	48	22	22	18	18	22	22	28	28
Si	10.3	11.6	7.95	8.00	5.47	5.32	5.03	5.03	6.29	6.06	5.30	5.35
Al ^{IV}	5.72	4.39	0.05		2.53	2.68	0.97	0.97	1.71	1.94	2.70	2.65
Al ^{VI}			17.5	17.5	0.89	0.74	2.97	2.99	3.57	3.77	2.92	2.86
Fe ³⁺			0.49	0.53								
Ti			0.03	0.01	0.12	0.08						0.01
Cr			0.01		0.03	0.02					0.01	0.06
Mg			0.81	0.89	2.96	3.24	1.46	1.48	0.56	0.23	5.84	5.97
Fe ²⁺		0.01	2.34	2.27	1.74	1.94	0.48	0.46	0.32	0.12	3.01	2.82
Mn ²⁺			0.11	0.10	0.01	0.02	0.02	0.01			0.03	0.02
Ca	1.63	0.38			0.01	0.01	0.01		0.06		0.02	0.01
Na	2.32	3.57			0.10	0.06	0.14	0.09	0.10	0.36		0.01
K	0.01				1.74	1.62			1.04	1.56	0.12	0.18
xK [Or]	0.00	0.01										
xNa [Ab]	0.59	0.90										
xCa [An]	0.41	0.09										
xFe[fcel]									0.14	0.06		
xMg[mcel]									0.25	0.11		
xAl[mphen]									0.61	0.83		

Sample	M1 (greenstone from the Murchison Unit)									
Mineral phase	Act	Act	Chl	Chl	Pl	Pl	Ep	Sph		
wt%										
Na ₂ O					11.7	11.9				
MgO	19.6	19.0	21.5	22.7						
Al ₂ O ₃	1.02	0.96	20.1	20.5	19.6	19.9	21.9	0.69		
SiO ₂	56.2	55.3	27.5	27.9	67.5	67.4	36.8	30.6		
K ₂ O					b.d.l.	b.d.l.				
CaO	13.0	13.1			0.12	0.20	23.13	29.0		
TiO ₂	b.d.l.	0.16	b.d.l.	0.16				37.9		
Cr ₂ O ₃	0.52	0.18	0.34	0.21				0.26		
MnO	0.26	0.23	0.23	0.19						
FeO	8.53	9.70	17.58	17.92				0.41		
Fe ₂ O ₃					b.d.l.	0.30	15.0			
Total	99.1	98.6	87.2	89.6	98.8	99.7	96.8	98.8		
Oxygens	23	23	28	28	32	32	13	5		
Si	7.82	7.79	5.59	5.52	11.9	11.9	3.10	1.01		
Al ^{IV}	0.17	0.16	2.41	2.48	4.08	4.12		0.03		
Al ^{VI}			2.39	2.30				2.17		
Fe ³⁺							0.03	0.95	0.01	
Ti		0.02		0.02					0.94	
Cr	0.06	0.02	0.05	0.03					0.01	
Mg	4.06	3.98	6.51	6.69						
Fe ²⁺	0.99	1.14	2.99	2.97		0.01	0.01			
Mn ²⁺	0.03	0.03	0.04	0.03						
Ca	1.94	1.97			0.02	0.04			1.02	
Na					4.00	4.04				
K										
xK [Or]										
xNa [Ab]					0.99	0.99				
xCa [An]					0.01	0.01				
x[cZo] = x[Zo]							0.09			

x[Ep]
x[Pie]

0.91
0.00

464

Sample	M2 (garnet- bearing aluminous quartzite of the Murchison Unit)							
Mineral phase	Gt	Gt	Bt	Bt	Chl	Chl	Wm	Wm
wt%								
Na ₂ O			0.07	0.09	0.04	0.03	0.93	1.06
MgO	2.31	1.80	7.12	7.99	8.85	8.65	0.73	0.81
Al ₂ O ₃	20.9	20.7	16.7	18.0	19.2	18.2	35.7	35.3
SiO ₂	36.7	36.4	39.8	36.6	30.0	32.7	46.5	46.6
K ₂ O			6.77	6.53	1.61	1.62	9.66	9.88
CaO	0.41	0.75	0.78	0.41	0.55	0.69	0.05	0.02
TiO ₂			1.16	1.31	0.08	0.04	0.18	0.34
Cr ₂ O ₃			0.15	0.12	0.10	b.d.l.	b.d.l.	0.21
MnO	4.63	6.06	0.16	0.13	0.23	0.32	0.01	0.02
FeO	35.5	34.6	19.9	18.4	27.7	23.5	1.4	1.2
Total	100.4	100.3	92.6	89.6	88.4	85.8	95.1	95.3
Oxygens	12	12	22	22	28	28	22	22
Si	5.95	5.95	6.10	5.79	6.34	6.92	6.17	6.18
Al ^{IV}	0.05	0.05	1.90	2.21	1.66	1.08	1.83	1.82
Al ^{VI}	3.96	3.93	1.11	1.13	3.13	3.46	3.76	3.70
Fe ³⁺	0.13	0.19						
Ti			0.13	0.16	0.01	0.01	0.02	0.03
Cr			0.02	0.02	0.02			0.02
Mg	0.56	0.44	1.63	1.88	2.79	2.73	0.14	0.16
Fe ²⁺	4.69	4.54	2.54	2.43	4.90	4.16	0.15	0.13
Mn ²⁺	0.64	0.84	0.02	0.02	0.04	0.06		
Ca	0.07	0.13	0.13	0.07	0.12	0.16	0.01	
Na			0.02	0.03	0.02	0.01	0.24	0.27
K			1.32	1.32	0.44	0.44	1.64	1.67
x[Py]	0.09	0.07						
x[Alm]	0.79	0.77						
x[Sps]	0.10	0.14						
x[Grs]	0.01	0.02						
xFe[fcel]							0.08	0.07
xMg[mcel]							0.07	0.08
xAl[mphen]							0.85	0.85

465

Sample	S (garnet- plagioclase- hornblende amphibolite from the Silwana Amphibolites)										
Mineral phase	Gt (core)	Gt (rim)	Hbl	Hbl in Gt	Bt	Bt	Pl	Pl	Ilm	Chl	Chl
wt%											
Na ₂ O			2.06	1.67	0.04	0.09	9.69	9.42		0.10	0.09
MgO	1.41	1.54	4.95	3.99	6.00	5.39			0.03	9.98	9.17
Al ₂ O ₃	20.6	20.5	14.0	13.3	16.0	16.3	22.3	22.7	0.00	19.7	14.2
SiO ₂	36.9	36.6	40.0	40.2	31.9	31.1	64.5	64.5		25.2	29.5
K ₂ O			0.56	0.41	6.63	5.23	0.04	0.08		0.13	1.85
CaO	4.94	5.26	10.4	11.0	0.02	0.14	3.55	3.58		0.13	0.24
TiO ₂			0.60	0.27	1.90	1.60			52.3	0.63	1.62
MnO	1.97	1.52	0.10	0.15	0.08	0.04	b.d.l.	b.d.l.	0.49	0.06	0.04
FeO	34.9	34.7	24.8	26.2	30.3	33.6			46.9	31.4	30.2
Fe ₂ O ₃							0.08	0.11			

hal-006691575, version 1 - 26 Apr 2012

Total	100.7	100.1	97.5	97.2	92.9	93.5	100.1	100.5	99.8	87.3	86.9
Oxygens	12	12	23	23	22	22	32	32	3	28	28
Si	5.97	5.95	6.25	6.3	5.26	5.14	11.4	11.3		5.52	6.50
Al ^{IV}	0.03	0.05	1.75	1.67	2.74	2.86	4.63	4.70		2.48	1.50
Al ^{VI}	3.89	3.87	0.82	0.80	0.36	0.31				2.62	2.19
Fe ³⁺	0.21	0.27					0.01		0.01		
Ti			0.07	0.03	0.24	0.20			1.00	0.10	0.27
Mg	0.34	0.37	1.15	0.94	1.47	1.33				3.26	3.01
Fe ²⁺	4.50	4.45	3.23	3.46	4.17	4.64		0.01	0.99	5.76	5.57
Mn ²⁺	0.27	0.21	0.01	0.02	0.01	0.01			0.01	0.01	0.01
Ca	0.86	0.92	1.74	1.86		0.02	0.67	0.67		0.03	0.06
Na			0.62	0.51	0.01	0.03	3.31	3.21		0.04	0.04
K			0.11	0.08	1.39	1.10	0.01	0.02		0.04	0.52
x[Py]	0.06	0.06									
x[Alm]	0.76	0.76									
x[Sps]	0.04	0.03									
x[Grs]	0.14	0.15									
xK [Or]							0.00	0.00			
xNa [Ab]							0.83	0.82			
xCa [An]							0.17	0.17			
xMg [Geik]									0.00		
xFe [Ilme]									0.99		
xMn [Pyro]									0.01		

Hal-06691575, version 1 - 26 Apr 2015, 66
 67
 68
 69
 70
 71
 72
 473
 474
 475

4. Metamorphic P—T paths

P—T paths for the different units were inferred by comparison between the observed mineral assemblages, mineral compositions and zoning patterns, and those obtained by P—T pseudosection calculations for the respective samples. This methodology provides robust results, as has been shown by many examples in the past; for example see Zeh et al. (2001, 2004); Millonig et al. (2008, 2010). The methods used to estimate the effective bulk rock composition and to construct P—T pseudosections are described in the Appendix (A2).

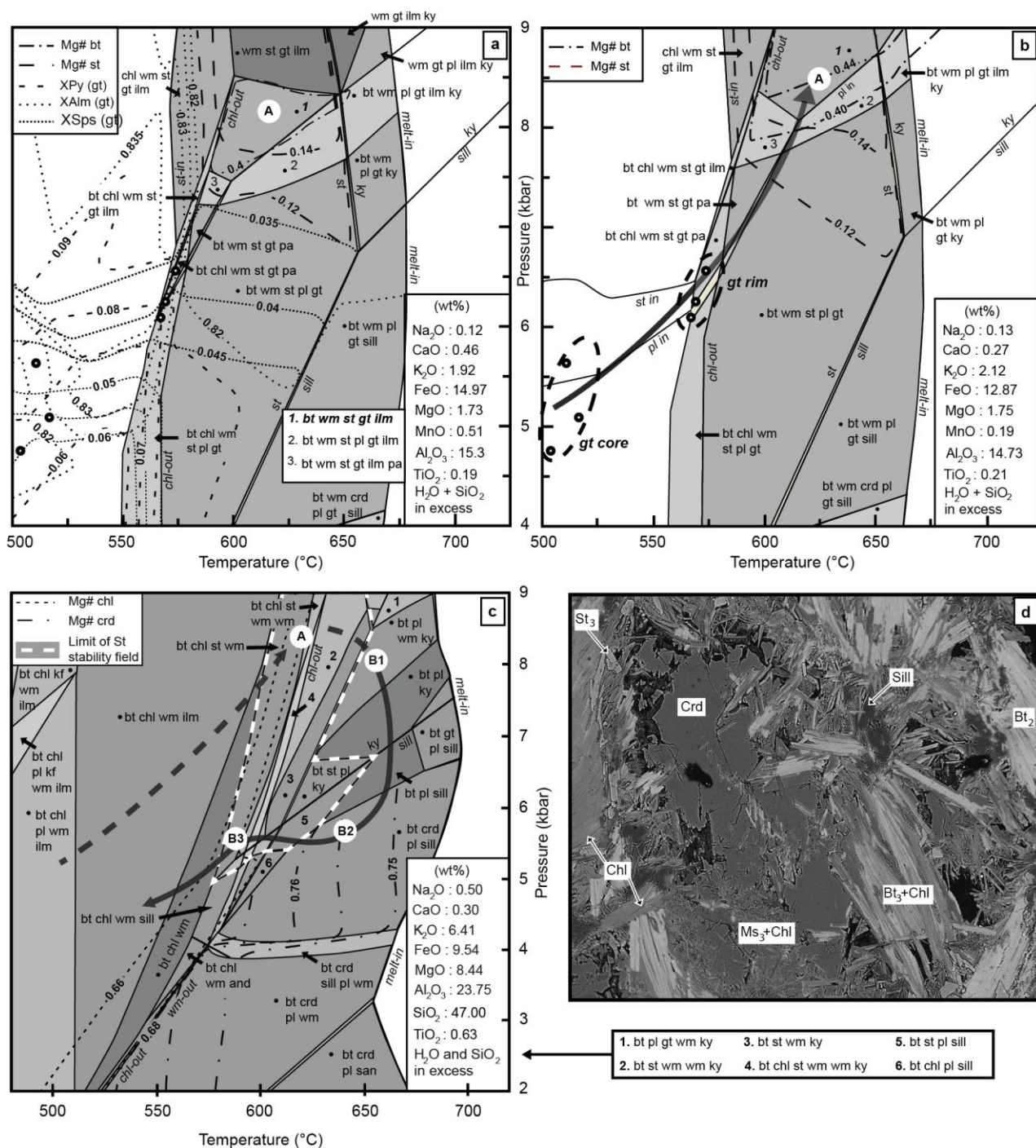


Figure 5:

P–T pseudosections for metapelitic rocks from the La France Formation, constructed in the model system (Mn)TiNCKFMASH (with H₂O and SiO₂ in excess). (a, b) P–T pseudosection for a garnet-staurolite micaschist (sample A) and (c) for a kyanite-bearing micaschist with retrograde cordierite and staurolite (sample B). The P–T pseudosection (a) is constructed by using the unfractonated bulk composition obtained by XRF analysis, and (b) is built by using the effective bulk composition after garnet growth ceased. Small open circles represent fit between calculated and measured garnet compositions, obtained from garnet cores and rims of zoned garnet in sample A. White circles labelled A, B1, B2, B3 mark the fields with the best agreement between observed and calculated mineral assemblages

486 and mineral compositions. The arrows define the P—T path inferred from the petrological constraints. (d)
487 SEM image of sample B showing tiny staurolite grains (St_3), which together with chlorite (Chl), biotite
488 (Bt_3) and muscovite (Ms_3) surround a cordierite (Crd) porphyroblast, intergrown with sillimanite (Sill)
489 and biotite (Bt_2). Wm = white mica.

491 **4.1. La France Formation**

492
493 P—T pseudosections for the La France Formation were calculated for a Gt-St-bearing schist (sample A)
494 and a Ky-St-Crd schist (sample B), which were collected about 300m apart. In the absence of any tectonic
495 break between the two outcrops we assume that both rocks underwent the same metamorphic history, and
496 consequently, that the different mineral assemblages and compositions result from different bulk rock
497 compositions. Thus a detailed P—T path can be constructed by superimposing the information obtained
498 from the different rock samples (e.g. Zeh et al., 2001, 2004; Reno et al. 2009).

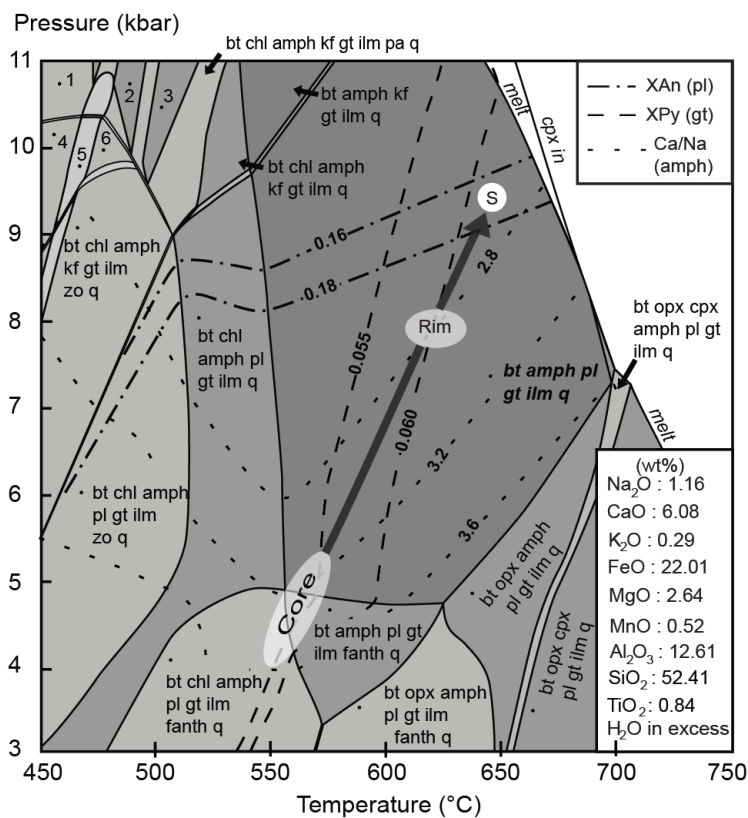
499
500 Results of P—T pseudosections for sample A (Fig 5a, b) indicate that the Gt-St-bearing schists of the La
501 France Formation experienced a prograde P—T increase from about 5.5 kbar, 520 °C to 7.5-9.0 kbar,
502 590-650 °C. The prograde P—T evolution is constrained by the agreement between observed and
503 calculated garnet zoning patterns, using the “garnet isopleths intercept method” (e.g., Evans 2004; Zeh et
504 al., 2006). The peak P—T conditions are determined from the correspondence between the calculated and
505 observed peak mineral assemblage (A): Grt + St + Bt_1 + Ms_1 + Q, and related mineral compositions. It
506 should be noted, however, that the fit between calculated and observed peak mineral compositions is not
507 perfect, i.e. the calculated mineral compositions of garnet rims plot outside the phase field for the peak
508 mineral assemblage (Fig. 5). This discrepancy may be explained by at least two reasons. Firstly, minerals
509 in sample A underwent a retrograde equilibration (causing a change of the peak mineral composition of
510 garnet rims and of biotites; e.g. Florence & Spear, 1991), and/or secondly, by internal fractionation,
511 causing a change of the effective bulk composition during prograde garnet growth (e.g. Stüwe, 1997;
512 Marmo et al., 2002; Zeh et al., 2006). The effects of chemical fractionation due to garnet growth are

513 modelled in Fig 5. Assemblage (A) is shifted from 7.5-8.5 kbar , 590-645°C for the unfractionated rock
514 (Fig. 5a) to higher P—T conditions of 8.0-9.0 kbar , 600-650°C when fractionation is taken into account
515 (Fig. 5b).

516
517 The peak metamorphic assemblage (B1) $Ky_1 + Bt_1 + Pl + Ms_1 + Q \pm St_1$ observed in sample B requires
518 peak P—T conditions of 6.8-9.0 kbar at 630–650°C. Comparison of the peak metamorphic conditions for
519 sample B and the prograde P—T vector inferred for sample A indicates that the formation underwent a
520 limited heating after reaching peak pressure. Syn-D2 muscovite in sample B has a modal proportion <
521 1%, suggesting equilibration near the white mica-out reaction curve that limits the multivariant field at
522 lower pressures. Sillimanite overgrowth around kyanite and the finding of cordierite in assemblage (B2):
523 $Sill + Bt_2 + Crd + Pl + Q$, provide evidence for a nearly isothermal decompression to P—T conditions of
524 <6 kbar at 600-660°C during retrograde evolution (Fig. 5c.). Cordierite is partly replaced by an
525 assemblage including St, Sill, Bt, Ms and Chl (assemblage (B3): $St_3 + Bt_3 + Chl + Ms_3 + Q$, Fig. 5d.),
526 implying that the near isothermal decompression was followed by a near-isobaric cooling to <600°C at
527 ~5.5 kbar. The change in the P—T path from a near-isothermal decompression to a near-isobaric cooling
528 may correspond to the onset of the D₃ deformation event.

530 **4.2. Silwana Amphibolites**

531
532 Results of P—T pseudosection calculations indicate that the observed peak metamorphic assemblage (S):
533 $Gt + Hbl + Pl + Bt + Ilm + Q$ is stable over a wide P—T range at temperatures between 540 and 690°C
534 and pressures between 4.6 and >11 kbar (Fig. 6). A prograde P—T path is inferred by comparing the
535 observed and calculated mineral composition of garnet (cores and rims), amphibole inclusions in garnet
536 and matrix amphibole, as well as of matrix plagioclase. Intersecting the isopleths for these minerals
537 provides evidence for a P—T increase from ~4.5 kbar, 540 °C, to peak metamorphic conditions of 8.7-10
538 kbar at 630-670°C.



1.chl wm cpx gt ilm zo pa q 3.bt chl amph gt ilm pa q 5.chl wm amph kf cpx gt ilm zo q
 2.chl wm amph gt ilm pa q 4.chl wm kf cpx gt ilm zo q 6.chl wm amph kf gt ilm zo q

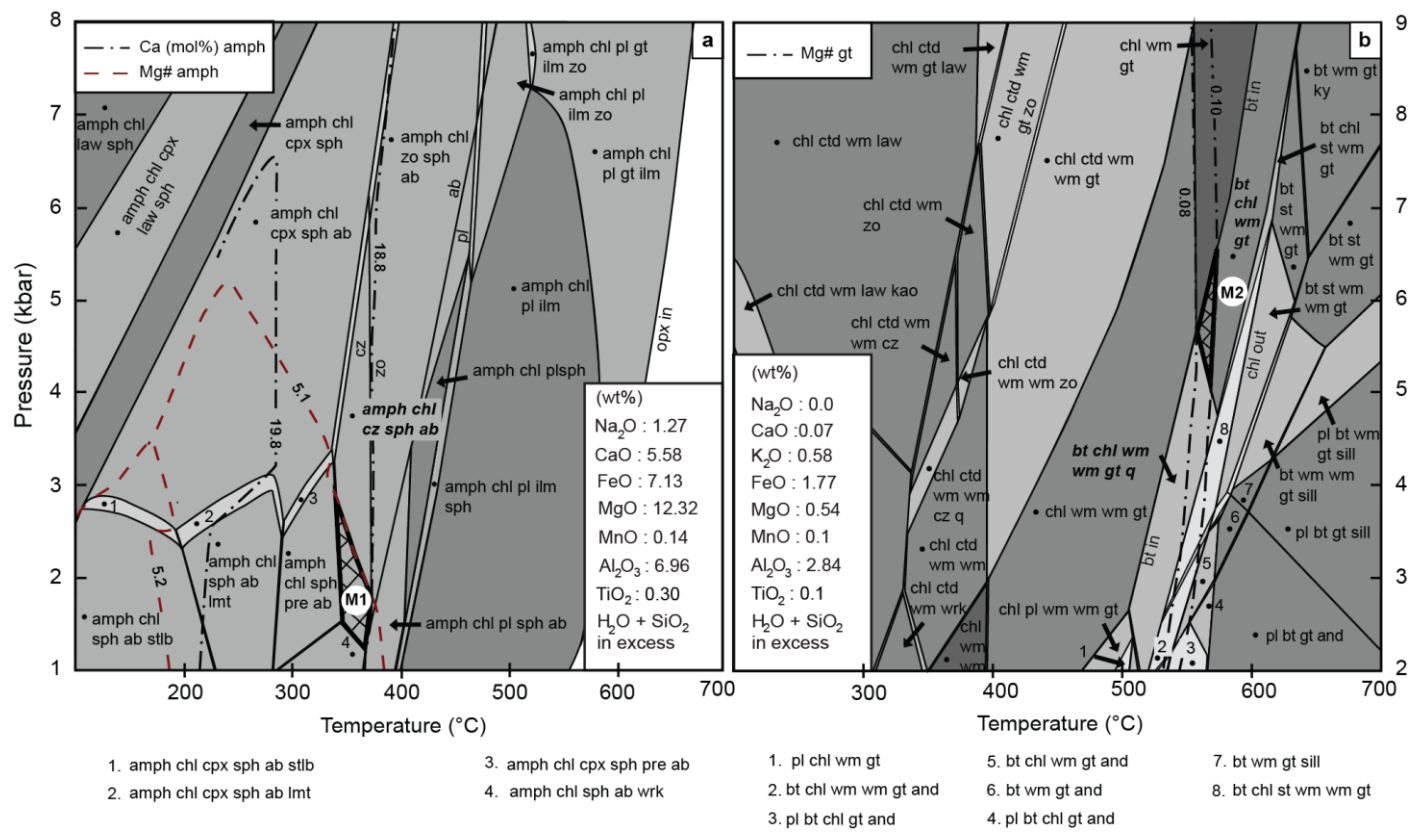
Figure 6:

P – T pseudosections for the Silwana Amphibolites. The pseudosection is constructed in the model system TiNCKFMASH system, with water in excess. White circles and ellipses mark the fields with the best agreement between observed and calculated assemblages and mineral compositions (core, rim, S). The multivariant field designated in bold-italics correspond to the observed peak assemblage. The arrows define the P–T vector inferred from petrological constraints. fanth = ferro-anthophyllite, pa = paragonite, zo = zoisite.

4.3. Murchison Unit

The model multivariant field corresponding to the metamorphic assemblage of sample M1: Act + Chl + Ab + Ep + Sph + Q (Fig. 7a) constrains metamorphic P–T conditions of 340-370°C at a wide pressure range from 1.3 to 5.8 kbar. The agreement between the measured and calculated actinolite composition restricts the metamorphic pressure conditions to 1.3-2.8 kbar at 340-370 °C (hatched field in Fig. 7a). However, it should be noted that clinozoisite (cz) instead of epidote has been calculated, due to the fact that the Fe³⁺ content was approximated to be 0 during the calculations (see Appendix A2). The observed

556 Mg# of chlorite falls in a P—T space characterised by even lower temperatures of 240 – 300°C (not
 557 shown). The latter may be indicative of chlorite (which is present in late-stage shear bands) crystallisation
 558 and/or re-equilibration during retrograde cooling. In summary, the geobarometric constraints for sample
 559 M1 point to a lower greenschist-facies metamorphism.



561 **Figure 7:**
 562 *P – T pseudosections for rocks from the Murchison Unit. (a) Metabasite from the center of the Murchison*
 563 *unit, sample M1. (b) Garnet-bearing aluminous quartzite from the southern edge of the Murchison Unit.*
 564 *Hatched areas labelled M1 and M2 mark the fields with the best agreement between observed and*
 565 *calculated assemblages and mineral compositions. Wm = white mica, and = andalusite, zo = zoisite, cz =*
 566 *clinozoisite, ab = albite, pre = prehnite, wrk = wairakite, lmt = laumontite, stlb = stilbite, kao =*
 567 *kaolinite.*

569 The P—T pseudosection constructed for the metapelite sample M2, containing the peak
 570 metamorphic assemblage (M2) Gt + Ms + Bt + Chl + Qtz , indicates peak temperatures between 530 and
 571 570 °C, at pressures between 5.0 and 6.2 kbar (hatched phase field in Fig. 7b). The peak metamorphic
 572 temperature conditions are constrained by two temperature-dependant field boundaries, the biotite-in and

573 chlorite-out / staurolite-in phase boundaries, as well as by the the fit between modelled and measured
574 Mg# of garnet (Fig. 7b). The finding of muscovite without other white micas in sample M2 furthermore
575 requires peak pressure conditions between 5.0 and 6.2 kbars at 550-570°C. The metamorphic grade of
576 sample M2 is somewhat higher than that of sample M1, at the transition between high T greenschist and
577 low P amphibolite facies, but is significantly lower than that of the rocks from the La France Formation
578 and Silwana Amphibolites.

581 **5. Geochronology**

582
583 In order to constrain the timing of metamorphism and deformation in the MGB, LA-ICP-MS U-Pb dating
584 was carried out on a syn-deformation granite intrusive in the Letaba Shear Zone (sample mur0982, see
585 Fig. 2 for location). In addition, monazite and xenotime from the kyanite-bearing metapelite from the La
586 France Formation (sample B) were dated.

587
588 The zircon grains were characterised by cathololuminescence imaging prior to analyses and were
589 analysed on grain mounts, while monazite and xenotime U-Pb analyses were carried out on a thin section,
590 after their characterisation by back-scattered electron imaging. The results are shown in Table 3 and in
591 Fig. 8. Analytical techniques and data processing methods are detailed in Appendix (A3).

594 ***5.1 Zircons from magmatic rocks***

595
596 Twenty zircons from the syn-deformation granite sample mur0982 intrusive into the LSZ to the North of
597 the belt, displaying an oscillatory magmatic zoning, were analysed. Nineteen out of twenty U-Pb analyses
598 plot along a discordia with an upper intercept at 2964 ± 5 Ma (MSWD = 5.4), whereas a xenocryst zircon

599 grain (28110411d) yields a much older $^{207}\text{Pb}/^{206}\text{Pb}$ age of 3251 ± 18 Ma (Table3). The upper intercept age
 600 is within error identical to a Concordia age (as of Ludwig, 1998) of 2964 ± 8 Ma (MSWD = 0.24,
 601 probability of concordance = 0.63, n=6) (Fig. 8a, b). It is interpreted to reflect the timing of the syn-
 602 tectonic granite emplacement. This interpretation is supported by the observation that the granite is
 603 intrusive in the Letaba Shear Zone and shows a mylonitic foliation that is coplanar with the mylonitic
 604 fabric of the greenschist-facies schists of the LSZ.

605
 606 *Table 3:*

607 *Top: U-Pb isotopic data obtained by LA-ICP-MS analyses carried out in GUF, and calculated ages from*
 608 *monazite and xenotime from sample B. Bottom: U-Pb isotopic data obtained by LA-ICP-MS analyses*
 609 *carried out in Clermont-Ferrand and calculated ages from zircons from sample mur0982.*

Results of U-Pb LA-ICP-MS analyses of monazite (mnz) and xenotime (xno) carried out at Goethe University Frankfurt

sample	$^{207}\text{Pb}^a$	U ^b	Pb ^b	Th ^b	$^{206}\text{Pb}^c$	$^{206}\text{Pb}^d$	$\pm 2\sigma$	$^{207}\text{Pb}^d$	$\pm 2\sigma$	$^{207}\text{Pb}^d$	$\pm 2\sigma$	rho ^e	^{206}Pb	$\pm 2\sigma$	^{207}Pb	$\pm 2\sigma$	^{207}Pb	$\pm 2\sigma$	conc. ^f	
	(cps)	(ppm)	(ppm)	U	(%)	^{238}U	(%)	^{235}U	(%)	^{206}Pb	(%)		^{238}U	(Ma)	^{235}U	(Ma)	^{206}Pb	(Ma)	(%)	
04	mnz	253119	847	2900	21.1	0.57	0.4804	4.1	12.54	4.1	0.1894	0.5	0.99	2529	86	2646	39	2737	8	92
05	mnz	536981	3062	6600	11.8	0.12	0.5312	2.0	14.00	2.1	0.1912	0.7	0.95	2747	45	2750	20	2752	11	100
06	mnz	370826	2627	4100	7.7	1.07	0.4852	2.6	12.77	2.8	0.1909	1.0	0.93	2550	55	2663	27	2750	17	93
07	mnz	519077	3342	5800	8.6	0.10	0.5504	2.4	14.53	2.5	0.1915	0.8	0.95	2827	54	2785	24	2755	12	103
core	xno	1149852	4946	3100	0.4	0.08	0.5562	8.1	16.11	8.2	0.2101	1.6	0.98	2851	189	2883	82	2906	26	98
10	xno	1255656	4462	2700	0.4	0.09	0.5249	4.4	14.71	4.8	0.2033	1.9	0.92	2720	98	2797	46	2853	30	95
12	mnz	630276	4092	8000	9.9	0.10	0.5122	2.1	13.43	2.2	0.1901	0.5	0.97	2666	46	2710	21	2743	9	97
13	mnz	105973	403	1300	19.7	1.73	0.3219	13.4	8.25	13.5	0.1860	1.3	1.00	1799	214	2259	130	2707	21	66
a14	mnz	445663	4136	7900	8.9	0.08	0.5231	2.8	13.85	2.9	0.1921	0.7	0.97	2712	63	2740	28	2760	12	98
a15	mnz	404074	2226	5300	13.9	0.19	0.5245	2.1	13.71	2.2	0.1896	0.5	0.97	2718	47	2730	21	2739	9	99
a16	mnz	382514	2406	4800	10.6	0.43	0.5344	2.1	14.09	2.2	0.1912	0.7	0.95	2760	48	2756	21	2753	11	100
a19	mnz	448130	2403	6000	13.8	0.35	0.5410	2.4	14.24	2.7	0.1909	1.1	0.91	2788	55	2766	26	2750	18	101
a20	xno	1314118	6201	3500	0.2	0.05	0.5305	1.9	14.00	2.0	0.1915	0.5	0.96	2743	42	2750	19	2755	9	100
a21	mnz	118475	661	2200	24.6	0.92	0.4411	5.5	11.26	5.9	0.1851	2.1	0.94	2356	110	2545	57	2699	34	87
a22	mnz	268818	2076	5100	13.5	0.13	0.5268	3.7	13.91	3.7	0.1916	0.4	0.99	2728	82	2744	35	2756	7	99
a23	mnz	392774	2528	5200	11.1	0.11	0.5416	2.0	14.39	2.4	0.1928	1.2	0.86	2790	46	2776	23	2766	20	101
a25core	mnz	897089	3654	10000	17.4	0.10	0.5697	2.0	16.67	2.1	0.2122	0.7	0.95	2906	48	2916	21	2923	11	99
a25rim	mnz	509831	2393	6200	14.6	0.10	0.5254	1.8	13.86	2.0	0.1913	0.7	0.94	2722	41	2740	19	2754	11	99
a26	mnz	161910	845	1600	9.3	0.74	0.4560	6.2	12.09	6.4	0.1922	1.4	0.98	2422	127	2611	62	2761	23	88
a27	mnz	358562	2024	4900	14.3	0.10	0.5352	1.6	13.95	1.7	0.1890	0.4	0.97	2763	36	2746	16	2734	6	101
a28	mnz	381917	2499	5700	12.2	0.39	0.4678	3.0	12.18	3.1	0.1888	0.8	0.96	2474	62	2618	30	2732	14	91
a29	mnz	585399	3991	8300	10.5	0.24	0.5010	2.4	13.48	2.5	0.1952	0.8	0.94	2618	52	2714	24	2786	14	94
a30	xno	1764628	8893	5200	0.3	0.03	0.5292	1.8	14.04	1.8	0.1924	0.5	0.96	2738	39	2752	18	2763	9	99
a31	xno	1374114	8166	4700	0.2	0.03	0.5338	2.5	14.20	2.6	0.1929	0.7	0.96	2757	57	2763	25	2767	12	100
a32	mnz	52970	149	550	20.0	0.66	0.5146	6.3	13.27	6.3	0.1870	0.9	0.99	2676	139	2699	62	2716	15	99
a33	mnz	415719	2602	5100	10.7	1.14	0.5317	2.4	13.92	2.5	0.1899	0.8	0.95	2748	54	2744	24	2741	13	100
a34	mnz	519221	2744	6700	13.9	0.06	0.5319	2.4	14.02	2.5	0.1912	0.6	0.97	2749	54	2751	24	2753	10	100
a35	mnz	174257	741	2800	24.4	0.92	0.4369	3.7	11.37	3.9	0.1888	1.0	0.97	2337	73	2554	37	2732	16	86

a36 mnz 286783 1597 4100 15.4 0.13 0.5326 2.4 14.01 2.5 0.1907 0.6 0.97 2753 54 2750 24 2749 9 100

^a Within run background-corrected mean ²⁰⁷Pb signal in cps (counts per second).

^b U and Pb content and Th/U ratio were calculated relative to GJ-1 reference zircon.

^c percentage of the common Pb on the ²⁰⁶Pb. b.d. = below detection limit.

^d corrected for background, within-run Pb/U fractionation (in case of ²⁰⁶Pb/²³⁸U) and common Pb using Stacy and Kramers (1975) model Pb composition and subsequently normalised to GJ-1 (ID-TIMS value/measured value); ²⁰⁷Pb/²³⁵U calculated using $\frac{^{207}\text{Pb}/^{206}\text{Pb}}{(^{238}\text{U}/^{206}\text{Pb}) \times 1/137.88}$

^e rho is the ²⁰⁶Pb/²³⁸U/²⁰⁷Pb/²³⁵U error correlation coefficient.

^f degree of concordance = $\frac{^{206}\text{Pb}/^{238}\text{U} \text{ age}}{^{207}\text{Pb}/^{206}\text{Pb} \text{ age}} \times 100$

611

Results of U-Pb LA-ICP-MS analyses of sample mur0982 carried out in Clermont Ferrand

		²⁰⁷ Pb ^a	U ^b	Pb ^c	Th ^b	²⁰⁶ Pb ^d	±2σ	²⁰⁷ Pb ^d	±2σ	²⁰⁷ Pb ^d	±2σ	rho ^e	²⁰⁶ Pb	±2σ	²⁰⁷ Pb	±2σ	²⁰⁷ Pb	±2σ	conc. ^f
		(cps)	(ppm)	(ppm)	U	²³⁸ U	(%)	²³⁵ U	(%)	²⁰⁶ Pb	(%)		²³⁸ U	(Ma)	²³⁵ U	(Ma)	²⁰⁶ Pb	(Ma)	(%)
mur0982																			
05110411d	zr	8180	39	23	0.20	0.5956	2.0	17.74	2.1	0.2161	2.2	0.94	3012	48	2976	21	2952	35	102
06110411d	zr	42538	408	126	0.38	0.3051	2.0	8.85	2.0	0.2103	2.1	0.97	1717	30	2323	18	2908	33	59
07110411d	zr	16914	98	47	0.24	0.4921	2.0	14.69	2.1	0.2165	2.1	0.96	2580	42	2796	20	2955	34	87
08110411d	zr	13025	73	35	0.20	0.5011	2.0	15.17	2.2	0.2195	2.3	0.92	2619	44	2826	21	2977	36	88
09110411d	zr	55162	669	157	0.47	0.2496	2.0	7.08	2.0	0.2058	2.1	0.97	1436	25	2122	18	2873	34	50
10110411d	zr	11560	67	32	0.32	0.5004	2.0	14.98	2.1	0.2171	2.2	0.94	2615	43	2814	20	2959	35	88
11110411d	zr	21853	318	70	0.53	0.2313	2.0	5.96	2.1	0.187	2.2	0.94	1341	24	1970	19	2716	36	49
12110411d	zr	11361	54	32	0.20	0.6084	2.0	18.27	2.2	0.2177	2.3	0.92	3064	50	3004	21	2964	36	103
15110411d	zr	15607	79	44	0.23	0.5785	2.0	17.42	2.1	0.2184	2.2	0.94	2943	48	2958	21	2969	35	99
16110411d	zr	22058	142	63	0.35	0.4593	2.0	13.75	2.1	0.2171	2.1	0.95	2437	41	2733	20	2960	34	82
17110411d	zr	20140	121	56	0.25	0.4916	2.0	14.82	2.1	0.2186	2.1	0.94	2578	43	2804	20	2971	34	87
18110411d	zr	12592	91	36	0.29	0.4169	2.0	12.36	2.2	0.2151	2.2	0.93	2246	39	2633	21	2944	35	76
19110411d	zr	14013	74	39	0.18	0.5605	2.0	16.91	2.2	0.2188	2.2	0.94	2869	47	2930	21	2972	35	97
20110411d	zr	9774	85	28	0.73	0.3431	2.1	10.32	2.2	0.2182	2.3	0.92	1902	34	2464	21	2968	36	64
21110411d	zr	9362	49	26	0.18	0.5792	2.1	17.40	2.2	0.2179	2.2	0.92	2945	49	2957	22	2966	36	99
22110411d	zr	10061	87	29	0.22	0.3513	2.1	10.53	2.3	0.2175	2.2	0.92	1941	35	2483	21	2962	36	66
25110411d	zr	12745	66	36	0.21	0.5848	2.1	17.65	2.3	0.2189	2.3	0.91	2968	49	2971	22	2972	36	100
26110411d	zr	11260	59	32	0.22	0.5851	2.1	17.58	2.3	0.2179	2.3	0.91	2969	49	2967	22	2966	36	100
27110411d	zr	8942	47	26	0.21	0.5872	2.1	17.52	2.4	0.2165	2.3	0.89	2978	50	2964	23	2955	37	101
28110411d	zr	21485	105	55	0.35	0.5329	2.1	19.16	2.3	0.2607	2.3	0.91	2754	47	3050	22	3251	35	85
29110411d	zr	25554	211	76	0.28	0.3868	2.1	11.33	2.3	0.2123	2.3	0.90	2108	38	2550	22	2924	37	72

^a Within run background-corrected mean ²⁰⁷Pb signal in cps (counts per second).

^b U and Pb content and Th/U ratio were calculated relative to GJ-1 reference zircon.

^c percentage of the common Pb on the ²⁰⁶Pb. b.d. = below detection limit.

^d corrected for background, within-run Pb/U fractionation (in case of ²⁰⁶Pb/²³⁸U) and common Pb using Stacy and Kramers (1975) model Pb composition and subsequently normalised to GJ-1 (ID-TIMS value/measured value); ²⁰⁷Pb/²³⁵U calculated using $\frac{^{207}\text{Pb}/^{206}\text{Pb}}{(^{238}\text{U}/^{206}\text{Pb}) \times 1/137.88}$

^e rho is the ²⁰⁶Pb/²³⁸U/²⁰⁷Pb/²³⁵U error correlation coefficient.

^f degree of concordance = $\frac{^{206}\text{Pb}/^{238}\text{U} \text{ age}}{^{207}\text{Pb}/^{206}\text{Pb} \text{ age}} \times 100$

612

613 **5.2 Monazite and xenotime dating**

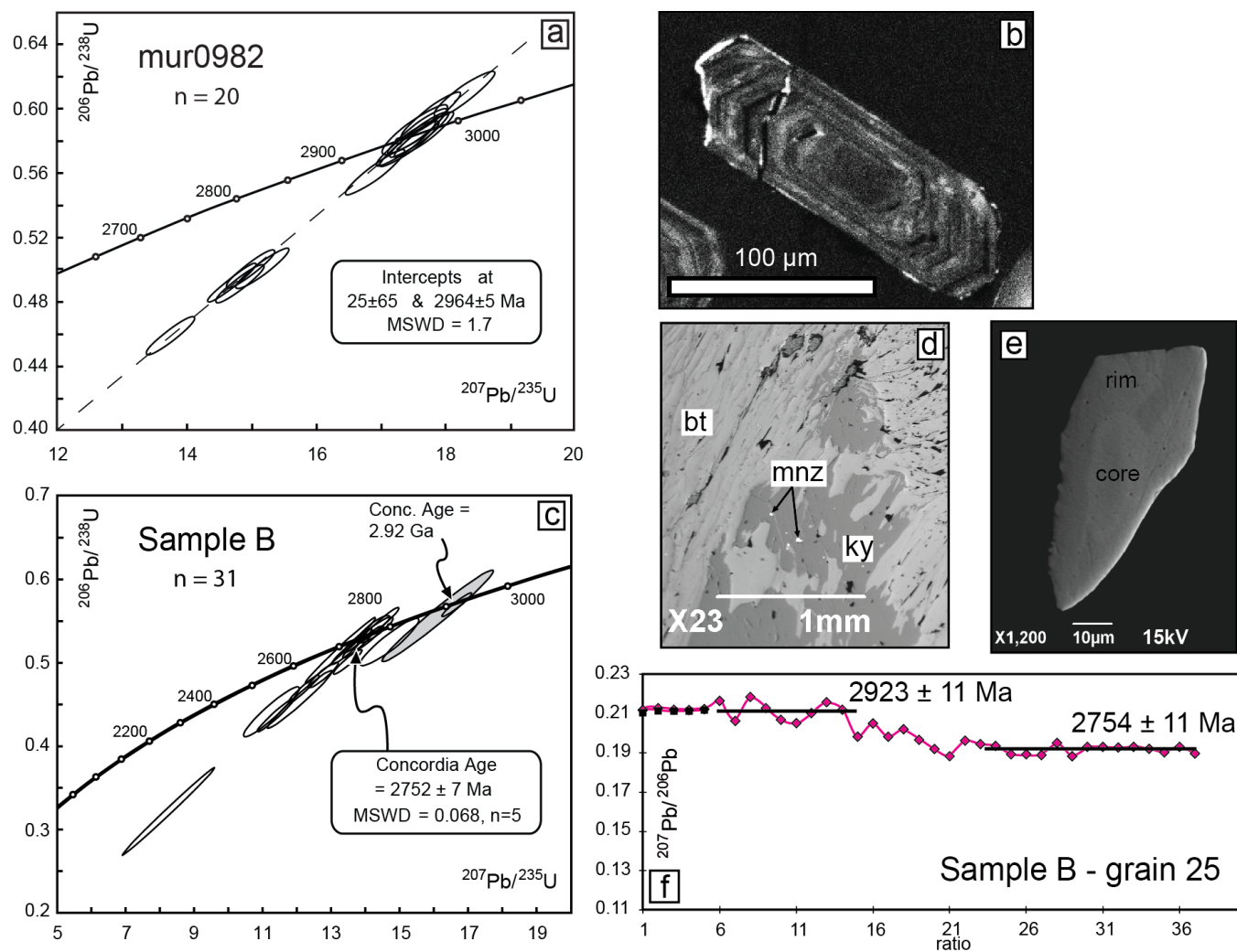
614

615 A total of 31 U-Th-Pb laser spot analyses were carried out on 18 monazite and 3 xenotime grains found in

616 the La France micaschists, sample B. The grains yielded two sets of concordant ages (Fig. 8c). Most

hal-00691575, version 1 - 26 Apr 2012

617 grains, which are intergrown with the matrix micas, yielded a concordant U-Pb age of 2752 ± 7 Ma.
 618 Xenotime and monazite inclusions in kyanite porphyroblasts yielded much older concordant U-Pb ages
 619 of 2906 ± 26 and 2923 ± 11 Ma, respectively (grey ellipses in Fig. 8c). The stepwise decrease of the time
 620 resolved, common Pb corrected $^{207}\text{Pb}/^{206}\text{Pb}$ signal during the analysis of the monazite inclusion in kyanite
 621 indicated that this grain was zoned. The drop of $^{207}\text{Pb}/^{206}\text{Pb}$ signal corresponds to an age decrease from
 622 2923 ± 11 Ma to 2754 ± 11 Ma (Fig. 8f). A possible explanation to this result is that kyanite and monazite
 623 formed at ca. 2923 Ma or prior to it, and that the monazite inclusion in kyanite subsequently underwent
 624 partial alteration and resetting at ca. 2754 Ma, simultaneous to the formation or complete re-
 625 crystallisation of matrix monazite and xenotime. We therefore suggest that the ca. 2923 Ma age represents
 626 a minimal age for the metamorphic peak in the La France Formation.



627 **Figure 8:**

628 **Results of U-Pb LA-ICP-MS dating of zircon, monazite and xenotime from the La France Formation.**

hal-00691575, version 1 - 26 Apr 2012

630 (a) Concordia diagram with results of U-Pb zircon dating of the granitoid sample mur0982 from the
631 Letaba Shear Zone. An upper intercept age of 2966.7 ± 7.1 Ma was obtained. (b) Cathodoluminescence
632 image of a zircon of sample mur0982. (c) Concordia diagram showing results of monazite and xenotime
633 analysis of sample B of the La France Formation, with concordant ages at 2752 ± 7 . (d) BSE image of
634 monazite inclusions in a kyanite porphyroblast in sample B. (e) BSE image of a monazite inclusion in
635 kyanite (sample B) revealing a complex zonation.
636 g) Time resolved $^{207}\text{Pb}/^{206}\text{Pb}$ signal obtained from a monazite inclusion in kyanite (mnz grain 25 - Table
637 3). Note the stepwise decrease of the $^{207}\text{Pb}/^{206}\text{Pb}$ signal, corresponding to an age decrease from $2923 \pm$
638 11 Ma to 2754 ± 11 Ma (2 sigma).

6. Discussion

6.1. Metamorphic conditions and geothermal gradients

The results of our P—T modelling reveal that the three investigated tectono-metamorphic units of the MGB underwent contrasted metamorphic evolutions. The volcano-sedimentary rocks of the Murchison Unit, that form the central part of the MGB, underwent metamorphism in the lower-greenschist to lower-amphibolite facies, at P—T conditions not exceeding 5-6.2 kbar and 530-570°C; peak metamorphic conditions being highly variable within this unit. In contrast, the La France Formation, on the southern edge of the MGB, underwent high grade amphibolite-facies metamorphism at conditions of 8 – 9 kbars, and temperatures of 600-650 °C, corresponding to higher-amphibolite facies conditions. They subsequently underwent near-isothermal decompression to under 6.2 kbar, with temperature between 600 and 660°C, followed by cooling to 570-610°C, at pressures in excess of 5 kbar. The Silwana Amphibolites sliver, on the north-western edge of the MGB, experienced a metamorphic overprint in the upper amphibolite facies under P—T conditions of 8.7 – 10 kbars, 630-670°C. Rocks of both units record a prograde pressure-temperature increase from about 4.5-5.5 kbars at 520-570°C towards the metamorphic peak. Furthermore, rocks of the La France Formation additionally provide evidence for a

658 complex retrograde P—T history, characterised by near-isothermal decompression from 9.0-6.8 to <6
659 kbar at 600-660 °C, followed by a nearly-isobaric cooling from 620-650 °C to 570-610°C at about 5.5
660 kbar, accompanied by a secondary H₂O-rich fluid enrichment.

661
662 Peak P—T conditions for the La France supracrustals and the Silwana Amphibolites require a
663 burial to mid-crustal levels, at depths of 27 – 30 km and 29 – 33 km respectively. Bearing in mind that the
664 pressures determined from peak assemblages are in fact minimal pressures due to possible re-
665 equilibration of the thermodynamic systems along the high-grade portions of the retrograde path, these
666 values represent minimal burial depths. Therefore, the La France Formation and the Silwana
667 Amphibolites underwent metamorphism along fairly similar minimal apparent geothermal gradients of
668 19-24°C/km. Furthermore, a steep prograde P—T vector inferred for rocks from both formations,
669 suggesting a fast burial. In contrast, much lower peak P—T conditions of 5-6.2 kbar and 550-570°C for
670 sample M2 indicate that rocks of the Murchison Unit were buried at shallower depths of 16 – 20 km,
671 along an apparent geotherm of 27-34 °C/km. The peak P—T conditions of metabasite sample M1 are
672 even lower and require even higher apparent geotherms (40-80°C/km). The reasons for the different peak
673 P—T conditions of the investigated rocks of Murchison Unit are not entirely clear. Apart from the fact
674 that the peak pressures are not well constrained, in particular for sample M1, the enormous temperature
675 differences could reflect either a metamorphic array (e.g. England & Thompson, 1984), whereby different
676 slivers has reached different peak conditions at different times or, alternatively, a metamorphic gradient
677 caused by magma intrusions within the MGB. A less likely option is that the enormous temperature
678 difference represents an artefact of the used thermodynamic calculation method. If the latter holds true,
679 the P—T results obtained from the metapelitic rocks are considered to be more appropriate than those
680 from the metabasite, since thermodynamic activity models for metapelite phases are more robust and less
681 sensitive to slight variations in Na, Ti and Fe³⁺ than those for metabasite phases, e.g. amphiboles (see
682 Dale et al., 2005; Diener et al. 2007; Diener and Powell, 2010).

683 It is interesting to note that the maximum peak P—T conditions obtained for the Murchison Unit

684 (5.0-6.2 kbars at 530-570 °C) overlap with those inferred from the retrograde P—T evolution of the La
685 France Formations (assemblage B3). Despite this coincidence, it remains unclear, whether the identical
686 P—T conditions in both units were reached at the same time, meaning that prograde heating in the
687 Murchison Unit ceased while rocks of the La France Formation underwent isothermal decompression. In
688 any case, our results show that the three tectono-metamorphic units of the MGB were buried along
689 different apparent geotherms, at different crustal depths, and experienced contrasted metamorphic
690 evolutions before being juxtaposed.

692 **6.2. Timing of the evolution of the MGB**

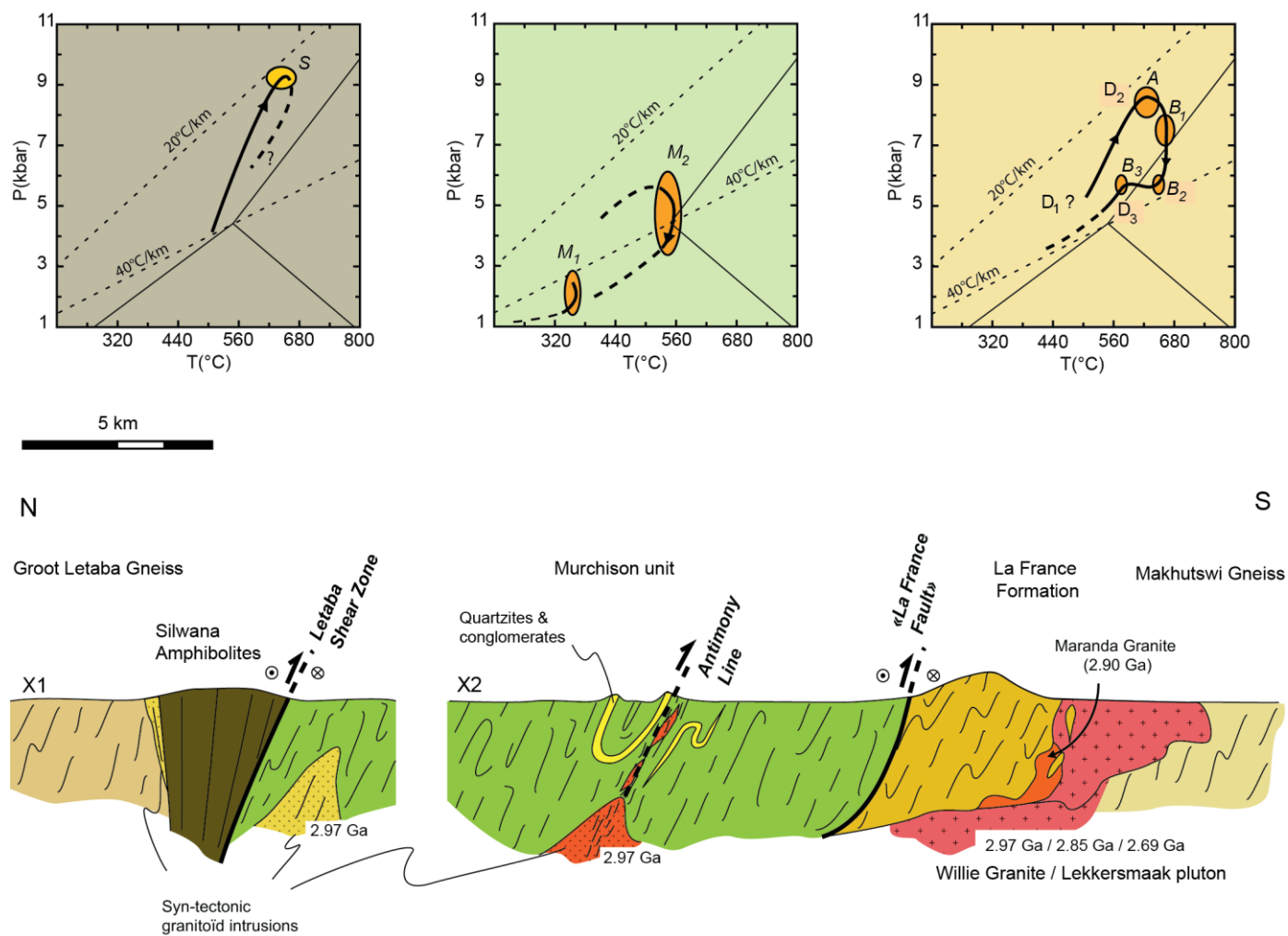
693
694 A maximum age for metamorphism in the Murchison Unit is provided by the youngest (meta)volcanic
695 rocks of the Rubbervale Formation of the MGB, dated at ca. 2.97 Ga (Brandl et al. 1996, Poujol et al.
696 1997, Poujol 2001). This age is identical within errors to the crystallisation age measured for the syn-
697 deformation granitoid intrusive in the Letaba Shear Zone. It also is indistinguishable from the
698 crystallisation ages of small granitoid bodies emplaced both along the Antimony Line (2970 ± 15 Ma
699 Malati Pump granodiorite, Poujol et al. 1997), and to the south of the MGB (2969 ± 17 Ma Discovery
700 granite, Poujol 2001). However, it is significantly older than the U-Pb ages of 2752 ± 7 Ma, and rarely of
701 2910-2920 Ma, obtained from the monazites and xenotimes of the La France micaschists. The older ages
702 of ca. 2.92 Ga which were only obtained from monazite or xenotime inclusions in kyanite, are interpreted
703 to reflect a minimum age for peak metamorphism in the La France Formation. It is worth noting that these
704 ages are within error identical to the emplacement age of the post-deformation Maranda Granite which
705 intruded the southern part of the MGB at 2901 ± 20 Ma (Poujol et al., 1996), pointing to a possible
706 synchronism of magmatism and metamorphism. The younger monazite and xenotime age of 2752 ± 7 Ma
707 may result from re-activation of the MGB related to thermal processes in the Rooiwater Complex of the
708 MGB (minimal intrusion ages of 2740 ± 4 Ma: Poujol et al., 1996), or in the Pietersburg Greenstone Belt
709 (intrusion of the Turfloop granite at ca. 2780 Ma; Henderson et al., 2000).

6.3. Deformation localisation along major tectonic breaks

The break in metamorphic conditions between the Silwana Amphibolites and the Murchison Unit greenschists requires a 9-23 km vertical displacement across the Letaba Shear Zone. Strain increases sharply from moderately deformed greenschists of the Murchison Unit to intensely sheared mylonites, to the amphibolitic gneiss of the Silwana Amphibolites. Furthermore, there is a marked change in deformation patterns across the shear zone, with a high-grade metamorphic flattening fabric, that formed during prograde metamorphism, in the Silwana Amphibolites, and low grade greenschist-facies mylonitic fabric, consistent with a sinistral strike-slip deformation, dominating in the Murchison Unit schists. The fabrics of the Letaba Shear Zone provide evidence for a general transpressive tectonic setting with a top-to-the-south transport. The structures observed in the Letaba Shear Zones suggest that the Silwana Amphibolites, formed at a low crustal level, were juxtaposed to the greenschist- to lower amphibolite-facies rocks of the Murchison Unit along a transpressive shear zone, that was activated due to sustained crustal shortening in a general N-S direction, and that accommodated a large vertical displacement. As crustal shortening and thickening were ongoing, the tectonic regime may have shifted from transpression with a strong reverse component and a top-to-the-south directed transport, to strike-slip shearing. Locally, conjugated SE-trending shear zones were activated together with the predominant NE-trending structures. This late stage of tectonic activity was accompanied by the intrusion of syntectonic granitoids in the Letaba Shear Zone at 2967 ± 7 Ma. These granitoids intruded prior to or during the sinistral slip under greenschist-facies conditions, as is well reflected by the S-C fabrics they display.

The La France Fault displays a number of similarities with the Letaba Shear Zone. It localises an important amount of deformation that accounts for a large vertical displacement of 7-20 kilometres. The fault zone also develops tectonic fabrics consistent with a general transpressive, sinistral regime and a

736 top-to-the-south transport direction. Deformation in the La France Formation shows patterns that are not
 737 seen elsewhere in the MGB. Deformation in the fault zone can be correlated with the D_3 deformation
 738 within the La France Formation, which is characterised by crenulations and small-wavelength open folds
 739 with shallow dipping axes. It post-dates the prograde P — T evolution of the La France Formation during
 740 the D_1 and D_2 deformation events. The structures of both shear zones illustrate a north-overriding-south
 741 relation.



742
 743 **Figure 9:**
 744 *Interpretative cross-section of the MGB. The MGB has an asymmetric structure, and structural units with*
 745 *distinct metamorphic P - T evolutions (see P — T diagrams) are juxtaposed along shear zones. The MGB*
 746 *is intruded by both syn-tectonic granitoids at 2.97 Ga and by late-stage granitoids as from 2.90 Ga. Profile*
 747 *lines labelled $x1$ and $x2$ are located on Fig. 2. Ellipses in the P — T diagrams indicate peak metamorphic*
 748 *and retrograde conditions obtained in this study.*
 749 *Dark solid curves represent P — T path segments inferred from our results of P — T modelling, while*
 750 *dashed curves show presumed portions of the paths. Deformation events (D_1 , D_2 , D_3) and studied*

751 *assemblages (S, M₁, M₂, A, B₁, B₂, B₃) are shown along the P—T paths.*

753 **6.4. Model of the tectono-metamorphic evolution of the MGB**

754
755 The structural-metamorphic data obtained during this study, along with previous works (e.g.,
756 Vearncombe, 1988a, 1988b; Jaguin et al., 2012) indicate that the different units of the MGB underwent a
757 similar style of penetrative, left-lateral deformation, as well as deformation localisation along the
758 boundaries between units with contrasted metamorphic evolutions (Fig 9). These features could be
759 accounted for by a sequential evolution model as follows: During the early stage of the evolution of the
760 MGB, shortening was accommodated by crustal thickening due to thrusts and/or transpressive shear zone
761 activation, whereby the different units underwent prograde metamorphism upon burial at lower to mid-
762 crustal level, along moderate apparent geothermal gradients. At some point during the thickening-
763 shortening process, the reverse component of the shear zones attenuated, as they evolved into a strike-slip
764 regime. Shortening was no longer accommodated solely along the primary shear zones that localised
765 deformation, but rather by a penetrative deformation distributed in the rocks of the MGB and surrounding
766 terrains, and homogeneous, moderate crustal thickening, coincident with a metamorphic overprint along a
767 high-T, low-P apparent geothermal gradient. Our results allow to suggest that the tectonic juxtaposition of
768 the Murchison Unit and La France Formation took place following crustal thickening, after peak
769 metamorphism and partial exhumation of the La France Formation, at which point the latter and a portion
770 of the Murchison Unit underwent a similar metamorphic evolution. The greenschist-facies metamorphism
771 of the Murchison Unit may have been locally overprinted by a slightly higher-grade metamorphism as a
772 consequence of tectonic accretion. Similarly, the final juxtaposition of the Silwana Amphibolites to the
773 rest of the belt occurred after peak metamorphism and exhumation, along a late-stage strike-slip shear
774 zone.

776 **6.5. Implications for Archaean tectonic regimes**

777
778
779
780
781
782
783
784
785
786
787
788
789
790
791
792
793
794
795
796
797
798
799
800
801
802

It is generally assumed that a higher average geothermal gradient prevailed in Archaean lithospheres relative to modern ones, thus maintaining weak lithospheres unable to withstand thickening (e.g. Rey and Houseman, 2006). Furthermore, a hot, more buoyant sub-continental lithospheric mantle in the Archaean (Griffin et al., 1998) would have inhibited lithosphere thickening by stacking in Archaean collisional belts, as it would have enhanced gravitational potential energy build-up as relief formed. Therefore, in an Archaean context, it is expected that convergence be accommodated by moderate thickening in its early stage, but quickly volume forces would become dominant on boundary stresses as gravitational potential energy builds up with increased thickening. Further thickening would be limited, and shortening would be accommodated by lateral escape of material, leading to a steady state where lithospheric thickness remains constant as long as convergence goes on (Rey and Houseman, 2006). This shift between the dominance of boundary stress to volume forces would correspond to the transition from a tectonic regime dominated by oblique thrusting to one marked by strike-slip shearing. It has been recognised in the sequential evolution of a number of Archaean and Palaeoproterozoic orogens (e.g. Kusky and Polat, 1999, in the Superior province, Feybesse et al., 2006 in the Birimian of the West African Craton). On Archaean lithospheres, the threshold controlling this transition would be reached much earlier than in Phanerozoic orogens, thus aborting pronounced thickening.

The cold apparent geothermal gradients inferred for the La France Formation and Silwana Amphibolites of the Murchison Greenstone Belt are comparable to those encountered in collisional belts in Proterozoic and Phanerozoic orogens (Brown, 2009). Burial along low geothermal gradients to about 30 km implies that the lithosphere strength was sufficient to sustain substantial thickening and loading, at least for a period of time. Weakening of the crust could therefore not have occurred before burial of supracrustal sequences at mid-crustal depths. In fact, the P–T paths followed by the La France Formation and the Silwana Amphibolites (Fig 9) inferred from our result are at odds with P–T paths expected from metamorphic terrains in hot orogens (Chardon et al, 2009; Gapais et al, 2009). Indeed, P–T paths

803 followed by particles in hot orogens are reported to show cooling during decompression, a sign that
804 exhumation is slow enough to enable thermal reequilibration (e.g., P-T paths from the Limpopo Belt: Zeh
805 et al., 2004; Millonig et al., 2010). In contrast, the Silwana Amphibolites and La France Formation
806 underwent a relatively fast burial, as is indicated by steep prograde P-T vectors, followed, for the latter,
807 by a near-isothermal decompression. These features suggest that isotherms were not parallel to the surface
808 at the time of metamorphism, and consequently exhumation must have been driven by tectonic processes
809 rather than by homogeneous erosion. An intermediate model between typical Archaean and Phanerozoic
810 orogens, where crustal shortening is accommodated by moderate crustal thickening, by deformation
811 localisation along transpressive shear zones, as well as by strike-slip shearing and strain distribution at a
812 regional scale, would better account for the tectono-metamorphic features of the MGB (e.g. Cagnard et
813 al., 2011).

814 The results of this study echo the metamorphic conditions reported in the south of the older, 3.5 – 3.2 Ga,
815 Barberton Greenstone Belt (Dziggel et al., 2002 ; Diener et al., 2005 ; Moyen et al., 2006). The tectono-
816 metamorphic evolution of the BGB shows similar thermal and mechanical properties of the lithosphere of
817 the Kaapvaal Craton before the formation of the MGB. It therefore seems likely that the Kaapvaal Craton
818 was a rather cold craton compared to other Archaean provinces, thus illustrating certain variability in
819 geodynamic processes within the Archaean.

822 **7. Conclusion**

823
824 The Murchison Greenstone Belt is a narrow volcano-sedimentary belt comprising various terrains that
825 have been tectonically juxtaposed. The geological units that represent most of the belt underwent lower-
826 greenschist to lower-amphibolite facies metamorphism along a relatively hot, ~30°C/km apparent
827 geothermal gradient. Two small slivers, at the north-eastern and southern edges of the MGB respectively,
828 were metamorphosed in the higher amphibolite facies. They underwent burial at more than 30 km deep

829 along a relatively cold, $\sim 20^{\circ}\text{C}/\text{km}$ geotherm. The contact zones between the low-grade and high-grade
830 formations are narrow and sharp. They represent high-strain shear zones that account for major breaks in
831 metamorphic conditions across the belt. While deformation due to shortening is distributed at a regional
832 scale, we show that shortening was also accommodated by localisation of deformation along
833 transpressive, sinistral tectonic contacts accompanied by a top-to-the-south directed transport. This mode
834 of shortening accounted for the final juxtaposition of terrains that were metamorphosed at different
835 crustal levels in the MGB.

836 The evolution of orogenic belts during shortening, from a tectonic regime dominated by thrusting,
837 thickening, and deformation localisation coincident with prograde metamorphism, to one dominated by
838 strike-slip shearing, lateral flow and deformation distribution accompanied by retrograde metamorphic
839 overprints, is not specific of or restricted to any time period in the geological record. As shown by our
840 results and by studies of the Barberton Greenstone Belt, moderate thickening, high-P, moderate- to low-T
841 metamorphism and high metamorphic gradients do occur in the Archaean. However, secular changes in
842 the heat budget of the Earth must have affected the relative importance of the different modes of
843 shortening, and probably account for the clearly contrasting tectonic features between the Archaean and
844 Proterozoic eras. In any case, drawing geodynamic models illustrating the differential behaviour of
845 Archaean and Proterozoic orogens should not be done without a consideration for the possible variations
846 of the parameters determining the rheological profiles and, as a consequence, the behaviour of
847 lithospheres at a given age.

849 **Appendix**

851 **A.1. XRF and microprobe analysis**

852
853 Whole rock chemistry analyses were obtained using an ACME at University of Stellenbosch, South
854 Africa. Complementary analyses were obtained by XRF at the CRPG in Nancy and the at the Ecole des

855 Mines in Saint-Etienne. Mineral chemical analyses were performed on a LEO 140VP scanning electron
856 microscope coupled to a Link ISIS energy dispersive spectrometry system at the University of
857 Stellenbosch. The microscope was operated at 20 kV with a beam current of 120A and a probe current of
858 1.5 nA. Acquisition time was set at 50 s and spectra were processed by ZAF corrections and quantified
859 using natural mineral standards. Details of the analytical procedure are provided in Diener et al. (2005).
860 Complementary analyses were carried out at the Electron Microprobe Laboratory at Université Blaise
861 Pascal in Clermont-Ferrand, France, using a Cameca SX 100 electron microprobe analyser. Operating
862 conditions were 20 kV, 20 nA, 5–10 µm beam size and counting time of 10s per element. Natural silicates
863 were used as standards. The analyses carried out in the different laboratories were identical within errors.

864 865 866 **A.2. Pseudosection calculation**

867 Pseudosections of rocks from the different terrains of the MGB were constructed using the
868 Peple_X software (Connolly and Kerrick, 1987; Connolly, 2005; 2009) in the Na₂O–CaO–K₂O–FeO–
869 (Fe₂O₃–)MgO–MnO–Al₂O₃–TiO₂–SiO₂–H₂O system, and using the thermodynamic database hp04 of
870 Holland and Powell (1998, revised 2004). The solution models used for the pseudosections are as follows
871 : Bio(TCC) for biotite (Tajcmanova et al., 2009), Chl(HP) for chlorite (Holland et al., 1998), St(HP) for
872 staurolite (Powell et al., 1998), Ctd(HP) for chloritoïd (Holland and Powell), Amph(DPW) for amphibole
873 (Dale et al., 2005), Gt(WPH) for garnet (White et al., 2000), Ilm(WPH) for ilmenite (White et al., 2000),
874 hCrd for cordierite, Mica(CHA1) for titanium bearing white mica (Coggon and Holland, 2002,
875 Auzanneau et al., 2010), Pheng(HP) for phengite (Holland and Powell 1998), melt(HP) (Holland and
876 Powell, 2001), Pl(h) for plagioclase feldspar (Newton et al. 1981), Kf for potassic feldspar (Waldbaum
877 and Thompson 1968), Opx(HP) for orthopyroxene (Holland and Powell, 1996), Cpx (HP) for
878 clinopyroxene (Holland and Powell, 1996). Pseudosections were first built by using the bulk rock
879 composition obtained by XRF analysis of each sample. However, this method failed to model accurately
880 the observed assemblages and mineral compositions for samples bearing large, centimetric minerals. For

881 such samples, the bulk rock composition was calculated from the mineral modes and average mineral
 882 compositions (e.g. samples A, B and S, Table 4). Modal proportions were estimated by image analysis,
 883 and average mineral compositions were obtained by averaging a large number of microprobe analyses
 884 acquired on minerals of a single thin section. In order to show the effect of garnet fractionation on the P—
 885 T pseudosection topology (e.g., sample A), we obtained the total bulk compositions by XRF, as well as
 886 the effective bulk composition after porphyroblast garnet growth, by subtracting the core composition of
 887 the zoned garnet grains (ca. 10 vol.%) from the total bulk composition, using a method similar to the
 888 procedure described by Marmo et al. (2002) and Zeh et al. (2006).

889

Whole rock XRF (wt%) - all Fe as Fe ²⁺						Recalculated (wt%)				
	A	B	M1	M2	S		A with Gt cores	A without Gt cores	B	S
SiO ₂	75.62	56.51	62.55	92.99	55.68	SiO ₂	61.67	64.24	47.00	52.41
Al ₂ O ₃	11.76	17.39	6.96	2.84	12.09	Al ₂ O ₃	15.30	14.73	23.75	12.61
FeO	6.68	8.08	7.13	1.77	16.21	FeO	14.97	12.87	9.54	22.01
MnO	0.04	0.07	0.14	0.10	0.18	MnO	0.51	0.19	0.00	0.52
MgO	1.52	8.45	12.32	0.54	2.77	MgO	1.73	1.75	8.44	2.64
CaO	< D.L.	0.52	5.58	0.07	7.19	CaO	0.46	0.27	0.30	6.08
Na ₂ O	0.17	0.61	1.27	0.00	2.89	Na ₂ O	0.12	0.13	0.50	1.16
K ₂ O	2.64	4.87	0.02	0.58	0.24	K ₂ O	1.92	2.12	6.41	0.29
TiO ₂	0.20	0.58	0.30	0.10	2.04	TiO ₂	0.19	0.21	0.63	0.84
P ₂ O ₅	0.17	b.d.l.	0.02	0.00	0.81	H ₂ O	1.50	1.50	sat.	sat.
LOI	2.35	2.99	3.40	1.06	0.89	Fe ₂ O ₃	0.00	0.00	0.00	0.00
Total	101.15	100.07	99.69	100.05	100.99	Total	98.37	98.01	96.57	98.56

890
891

892 *Table 4:*

893 *Whole rock compositions of the studied samples. The pseudosections of samples from the Murchison Unit*
 894 *(M1 and M2) were built using the whole rock compositions obtained by XRF analysis. Whole rock*
 895 *compositions were recalculated for the other samples to take into account the effect of large*
 896 *porphyroblasts on the composition of an equilibration volume (samples A, B and S) or to correct the effect*
 897 *of accessory phases (sample S, see appendix A2).*

898

899 Fe₂O₃ of the bulk rock was estimated by calculating the Fe³⁺ content of normalised structural formulae of
 900 analysed minerals (Droop, 1987) and from mineral modes. By applying this procedure we obtained Fe₂O₃
 901 contents of less than 0.05 wt% for all samples. T – X pseudosections were constructed to test the

902 implications of approximating all Fe as Fe^{2+} . In all cases, the consequences in terms of phase
903 compositions and proportions were found to be negligible. Thus, Fe_2O_3 as a system component was
904 ignored during this study, since it is little influential. Other corrections included correcting whole rock Ca
905 content for apatite and calcite in the studied sample, using calcite modal proportions and bulk P_2O_5
906 composition. As a general rule, oxides with a bulk rock content <0.05 wt% were ignored for
907 pseudosection calculations.

908 The prograde history of fluid-bearing mineral assemblages involves the progressive dehydration and fluid
909 loss with rising temperature. The water content of a rock decreases along the prograde path and reaches a
910 minimum at peak metamorphic conditions. Unless a secondary water enrichment occurs (such as
911 documented in sample B), the water content along the retrograde path is assumed to be close to the water
912 content at peak T conditions. As the retrograde assemblages of the investigated samples require a post-
913 peak metamorphism water influx, the P—T pseudosections for all samples were constructed under the
914 assumption that water was in excess throughout the entire metamorphic history.

915 **A.3. LA-ICP-MS U-Th-Pb dating**

916 A classic mineral separation procedure has been applied to concentrate zircon grains using the facilities
917 available at Géosciences Rennes. Rocks were crushed and only the powder fraction with a diameter < 250
918 μm was kept. Heavy minerals were successively concentrated by Wilfley table and heavy liquids.
919 Magnetic minerals were then removed with an isodynamic Frantz separator. Zircon grains were
920 handpicked under a binocular microscope and embedded in epoxy mounts. The grains were then hand-
921 grounded and polished on a lap wheel with a $6 \mu\text{m}$ and $1 \mu\text{m}$ diamond suspension successively. Zircons
922 were imaged by cathodoluminescence (CL) using a Reliotron CL system equipped with a digital color
923 camera available in Géosciences Rennes.

924
925
926 U-Th-Pb geochronology of zircon from the sample mur0982 was conducted by in-situ laser
927 ablation inductively coupled plasma mass spectrometry (LA-ICPMS) at the Laboratoire Magmas et

928 Volcans in Clermont-Ferrand, France, using a Resonetics M-50E 193 nm ArF excimer NewWave UP213
929 laser system, with a laser spot diameter of 26 μm and repetition rates of 3 Hz. Data were corrected for U-
930 Pb fractionation and for the mass bias by standard bracketing with repeated measurements of the GJ-1
931 zircon (Jackson et al., 2004). Data reduction was carried out with the GLITTER® software package
932 developed by the Macquarie Research Ltd. (Jackson et al., 2004). Further information on the
933 instrumentation and the analytical technique is detailed in Hurai et al. (2010).

934
935 U-Pb dating of monazite and xenotime was carried out on polished thin sections at Goethe
936 University Frankfurt, Germany. Prior to the U-Pb dating, the internal structures of the grains were
937 investigated by back-scattered electron (BSE) imaging using a ThermoScientific Element 2 sector field
938 ICP-MS coupled to a Resolution M-50 (Resonetics) 193 nm ArF excimer laser (ComPexPro 102F,
939 Coherent) system. Data were acquired in time resolved – peak jumping – pulse counting / analogue mode
940 over 356 mass scans, with a 20 second background measurement followed by 21 second sample ablation.
941 Laser spot-size for monazite and xenotime are 15 μm , and 23 μm for the standard zircons GJ1. Ablations
942 were performed in a 0.6 L min^{-1} He stream, which was mixed directly after the ablation cell with 0.07 L
943 min^{-1} N_2 and 0.68 L min^{-1} Ar prior to introduction into the Ar plasma of the SF-ICP-MS. All gases had a
944 purity of >99.999% and no homogeniser was used while mixing the gases to prevent smoothing of the
945 signal. Signal was tuned for maximum sensitivity for Pb and U while keeping oxide production,
946 monitored as $^{254}\text{UO}/^{238}\text{U}$, below 0.5%. The sensitivity achieved was in the range of 9000-14000 cps/ $\mu\text{g g}^{-1}$
947 ^{238}U with a 23 μm spot size, at 5.5 Hz and 5-6 J cm^{-2} laser energy. The two-volume ablation cell
948 (Laurin Technic, Australia) of the M50 enables detection and sequential sampling of heterogeneous
949 grains (e.g., growth zones) during time resolved data acquisition, due to its quick response time of <1s
950 (time until maximum signal strength was achieved) and wash-out (< 99.9% of previous signal) time of
951 about 2s. With a depth penetration of $\sim 0.7 \mu\text{m s}^{-1}$ and a 0.46s integration time (4 mass scans = 0.46 s = 1
952 integration) any significant variation of the Pb/Pb and U/Pb in the μm scale is detectable. Raw data were
953 corrected offline for background signal, common Pb, laser induced elemental fractionation, instrumental

954 mass discrimination, and time-dependent elemental fractionation of Pb/U using an in-house MS Excel[®]
955 spreadsheet program (Gerdes and Zeh, 2006; 2009). A common-Pb correction based on the interference-
956 and background-corrected ²⁰⁴Pb signal and a model Pb composition (Stacey & Kramers 1975) was carried
957 out. The ²⁰⁴Pb content for each ratio was estimated by subtracting the average mass 204 signal, obtained
958 during the 20 second baseline acquisition, which mostly results from ²⁰⁴Hg in the carrier gas (c. 180-420
959 cps), from the mass 204 signal of the respective ratio. For the analyzed sample the calculated common
960 ²⁰⁶Pb contents was mostly <1% of the total ²⁰⁶Pb (see Table 3). For more details about data processing see
961 (Gerdes and Zeh, 2006; 2009). The data were plotted using the software ISOPLOT (Ludwig 2001).

963 **Acknowledgements**

964 The authors thank Michael Brown for his detailed review of the manuscript which contributed to improve
965 significantly the quality of the work. Timothy Kusky and an anonymous reviewer are also thanked for
966 their constructive comments. The participation of Arnaud Villaros through discussions and advice was
967 greatly appreciated. Preliminary results of this study were presented at the 5th International Archaean
968 Symposium in Perth in 2010 thanks to a travel grant provided by Geoconferences (WA) Inc. Armin Zeh
969 also thanks the Deutsche Forschungsgemeinschaft, grant ZE 424/11-1, for financial support.

972 **References**

- 973
- 974 Altermann, W. and Nelson, D.R., 1998. Sedimentation rates, basin analysis and regional
975 correlations of three Neoproterozoic and Palaeoproterozoic sub-basins of the Kaapvaal Craton,
976 Northern Cape Province, South Africa. *J. Afr. Earth Sci.*, **13**, 415-435.
- 977
- 978 Anhaeusser, C.R., 2006. A reevaluation of Archean intracratonic terrane boundaries on the Kaapvaal
979 Craton, South Africa: Collisional suture zones? *GSA Special Papers* 2006, 405 193-210

- 980
- 981 Auzanneau, E., Schmidt, M.W., Vielzeuf, D., Connolly, J.A.D., 2010. Titanium in phengite: a
982 geobarometer for high temperature eclogites. *Contrib. Mineral. Petrol.* 159, 1-24.
- 983
- 984 Berthé, D., Choukroune, P., Jegouzo, P., 1979. Orthogneiss, mylonite and non-coaxial deformation of
985 granites : the example of the South Armorican shear zone. *J. Struct. Geol.* 1, 31-43.
- 986
- 987 Binns, R.A., Gunthrope, R.J. and Groves, D.I., 1976. Metamorphic patterns and development of
988 greenstone belts in the eastern Yilgarn Block, Western Australia. In: Windley, B.F. (ed.). *The
989 Early History of the Earth.* Wiley, New York, N.Y., 303–316.
- 990
- 991 Bouhallier, H., Choukroune, P. and Ballevre, M., 1993. Diapirism, bulk homogenous shortening and
992 transcurrent shearing in the Archaean Dharwar craton: the Holenarsipur area. *Precambrian
993 Res.*, 63, 43–58.
- 994
- 995 Bouhallier, H., Chardon, D., Choukroune, P., 1995. Strain patterns in Archaean dome-and-basin
996 structures: the Dharwar craton (Karnataka, South India). *Earth Planet. Sci. Lett.* 135, 57–75.
- 997
- 998 Brandl, G., Kröner, A., 1993. Preliminary results of single zircon studies from various Archaean
999 rocks of the Northeastern Transvaal. In: *Ext. Abstr. 16th International Colloquium of African
1000 Geology, Mbabane, Swaziland*, 54–56.
- 1001
- 1002 Brandl, G., Jaeckel, P., Kröner, A., 1996. Single zircon age for the felsic Rubbervale Formation,
1003 Murchison greenstone belt, South Africa. *S. Afr. J. Geol.* 99, 3, 229–234.
- 1004
- 1005 Brandl, G., Cloete, M., Anhaeusser, C.R., 2006. Archaean Greenstone Belts, In: Johnson, M.R.,

1006 Anhaeusser, C.R., Thomas, R.J., The Geology of South Africa, 2006.

1007
1008 Brown, M., 2007. Metamorphic conditions in orogenic belts: a record of secular change. *Int. Geol.*
1009 *Rev.* 49:193–234

1010
1011 Brown, M., 2009. Metamorphic patterns in orogenic systems and the geological record. In: Cawood
1012 PA, Kroner A (eds) *Earth accretionary systems in space and time*, vol 318. *Geol. Soc. Lond. Spec.*
1013 *Publ.*, 37–74

1014
1015 Brown, M., 2010. Paired metamorphic belts revisited. *Gondwana Research* 18, 46–59.

1016
1017 Burger, A.J., Coertze, F.J., 1973. Radiometric age measurements on rocks from southern Africa to the
1018 end of 1971. *Bull. Geol. Surv. S. Afr.* 58, 46–46.

1019
1020 Caby, R., Delor, C., Agoh, O., 2000. Lithologie, structure et métamorphisme des formations
1021 birimiennes dans la région d'Odienné (Côte d'Ivoire): rôle majeur du diapirisme des plutons et
1022 des décrochements en bordure du craton de Man. *J. Afr. Earth Sci.* 30, 351–374.

1023
1024 Cagnard, F., Barbey, P., Gapais, D., 2011. Transition between “Archaean-type” and “modern-type”
1025 tectonics : Insights from the Finnish Lapland Granulite Belt. *Precambrian Res.* 187, 127–142.

1026
1027 Cawood, P., Kröner, A., Collins, W.J. et al., 2009. Accretionary orogens through Earth history. *Geol. Soc.*
1028 *Lond. Spec. Publ.*, 318, 1-36.

1029
1030 Chardon, D., Choukroune, P., Jayananda, M., 1996. Strain patterns, décollement and incipient sagducted
1031 greenstone terrains in the Archaean Dharwar craton (South India). *J. Struct. Geol.* 18, 991–1004.

1032
1033 Chardon, D., Choukroune, P., Jayananda, M., 1998. Sinking of the Dharwar basin (South India):
1034 implications for Archaean tectonics. *Precambrian Res.* 91, 15–39.

1035
1036 Chardon, D., Andronicos, C.L., Hollister, L.S., 1999. Large-scale transpressive shear zone patterns and
1037 displacements within magmatic arcs: the Coast Plutonic Complex, British Columbia. *Tectonics* 18,
1038 278–292.

1039
1040 Chardon, D., Jayananda, M., Chetty, T.R.K., Peucat, J.-J., 2008. Precambrian continental strain and
1041 shear zone patterns: South Indian case. *J. Geophys. Res.* 113, B08402,
1042 doi:10.1029/2007JB005299.

1043
1044 Chardon, D., Gapais, D., Cagnard, F., 2009. Flow of ultra-hot orogens: a view from Precambrian,
1045 clues for the Phanerozoic. *Tectonophysics* 477 (3–4), 105–118.

1046
1047 Chopin, C., 1984. Coesite and pure pyrope in high-grade blueschists of the western Alps: a first record
1048 and some consequences. *Contrib. Mineral. Petrol.* 86, 107–118.

1049
1050 Choukroune, P., Bouhallier, H., Arndt, N.T., 1995. Soft lithosphere during periods of Archean crustal
1051 growth or crustal reworking. In: Coward, M.P., Ries, A.C. (Eds.), *Early Precambrian Processes*.
1052 *Geol. Soc. Spec. Publ.*, 95, 67–86.

1053
1054 Choukroune, P., Ludden, J.N., Chardon, D., Calvert, A.J., Bouhallier, H., 1997. Archaean crustal growth
1055 and tectonic processes: a comparison of the Superior Province, Canada and the Dharwar craton,
1056 India. In: Burg, J.-P., Ford, M. (Eds.), *Orogeny through Time*. *Geol. Soc. Spec. Publ.*, 121, 63–98.

- 1058 Coggon, R., Holland, T.J.B., 2002. Mixing properties of phengitic micas and revised garnet-phengite
1059 thermobarometers. *J. Metamorph. Geol.* **20**, 683-96.
- 1060
- 1061 Collins, W.J., Vernon, R.H., 1991. Orogeny associated with anticlockwise P–T–t paths: evidence from
1062 low-P, high-T metamorphic terranes in the Arunta inlier, central Australia. *Geology* **19**, 835–838.
- 1063
- 1064 Compston, W., Kröner, A., 1988. Multiple zircon growth within early Archean tonalitic gneiss from the
1065 Ancient Gneiss Complex, Swaziland. *Earth Planet. Sci. Lett.* **87**, 13–28.
- 1066
- 1067 Connolly, J. A. D., 2005. Computation of phase equilibria by linear programming : A tool for geodynamic
1068 modeling and its application to subduction zone decarbonation. *Earth Planet. Sci. Lett.* **236**, 524-
1069 541.
- 1070 Connolly, J. A. D., 2009. The geodynamic equation of state : what and how. *Geochemistry, Geophysics,*
1071 *Geosystems* **10**.
- 1072
- 1073 Connolly, J. A. D. and Kerrick, D.M., 1987. An algorithm and computer program for calculating
1074 composition phase diagrams. *CALPHAD* **11**:1-
- 1075
- 1076 Condie, K. C. and Kröner, A., 2008. When did plate tectonics begin? Evidence from the geologic record
1077 in Condie, K. C. and Pease, V. eds. *When Did Plate Tectonics Begin on Planet Earth?* Geological Society
1078 of America Special Paper 440, 281-294, doi: 10.1130/2008.2440(14).
- 1079
- 1080 Dale, J., Powell, R., White, R.W., Elmer, F.L., Holland, T.J.B., 2005. A thermodynamic model for Ca-Na
1081 clin amphiboles in Na₂O-CaO-FeO-MgO-Al₂O₃-SiO₂-H₂O-O for petrological calculations. *J.*
1082 *Metamorph. Geol.* **23**, 771-91.

1083
1084 Diener, J.F.A, Stevens, G, Kisters, A.F.M, Poujol, M., 2005. Metamorphism and exhumation of the
1085 basal parts of the Barberton greenstone belt, South Africa: Constraining the rates of
1086 Mesoarchaeon tectonism. *Precambrian Res.*143, 87–112.
1087

1088 Diener, J.F.A., Powell, R., White, R.W., & Holland, T.J.B., 2007. A new thermodynamic model for clino-
1089 and orthoamphiboles in the system Na₂O-CaO-FeO-MgO-Al₂O₃-SiO₂-H₂O-O. *J. Metamorph.*
1090 *Geol.*, 25, 631-656.
1091

1092 Diener, J.F.A., Powell, R., 2010. Influence of ferric iron on the stability of mineral assemblages. *J.*
1093 *Metamorph. Geol.*, 28, 599–613.
1094

1095 De Wit, M., 2004. Archean greenstone belts do contain fragments of ophiolites. In Condie, K. C., Kusky,
1096 T. M. (Editors), *Precambrian Ophiolites and Related Rocks, Developments in Precambrian Geology v. 13*,
1097 Elsevier Publishers.
1098

1099 Droop, G.T.R., 1987. A general equation for estimating Fe³⁺ concentrations in ferromagnesian silicates
1100 and oxides from microprobe analyses, using stoichiometric criteria. *Mineralogical*
1101 *Magazine*, 51 (3), 361, 431-435.
1102

1103 Du Plessis, C. P., 1990. Tectonism along the Thabazimby-Murchison lineament. Ph.D. Thesis (unpubl.),
1104 Univ Witwatersrand, Johannesburg, 243 pp.
1105

1106 Dzigel, A., Stevens, G, Poujol, M., Anhaeusser, C.R., Armstrong, R.A., 2002. Metamorphism of
1107 the granite–greenstone terrane south of the Barberton greenstone belt, South Africa: an insight
1108 into the tectono-thermal evolution of the ‘lower’ portions of the Onverwacht Group.

1109 Precambrian Res. 114, 221–247.

1110
1111 England, P. C. and Thompson, A. B., 1984. Pressure – temperature – time paths of regional
1112 metamorphism, Part I; heat transfer during the evolution of regions of thickened continental crust.
1113 J. Petrol., 25, 894-928.

1114
1115 Ernst, W.G., 1973. Blueschist metamorphism and P – T regimes in active subduction zones.
1116 Tectonophysics 17, 255–272.

1117
1118 Ernst, W.G., 1975. Systematics of large-scale tectonics and age progressions in Alpine and circum-
1119 Pacific blueschist belts. Tectonophysics 26, 229–246.

1120
1121 Ernst, W.G., 1988. Tectonic history of subduction zones inferred from retrograde blueschist P – T paths.
1122 Geology 16, 1081–1084.

1123
1124 Evans, T. P., 2004. A method for calculating effective bulk composition modification due to crystal
1125 fractionation in garnet bearing schist: implications for isopleth thermobarometry. J.
1126 Metamorph. Geol. 22, 547–557.

1127
1128 Feybesse, J.-L., Billa, M., Guerrit, C., Duguey, E., Lescuyer, J.-L., Milesi, J.P., Bouchot, V., 2006. The
1129 paleoproterozoic Ghanaian province : Geodynamic model and ore controls, including regional stress
1130 modeling. Precambrian Res. 149, 149-196.

1131
1132 Florence, F. P. and Spear, F. S., 1991. Effects of diffusional modification of garnet growth zoning on P - T
1133 path calculations. Contrib. Mineral. Petrol., 107, 487-500.

- 1135 Gapais, D., Cagnard, F., Gueydan, F., Barbey, P., Ballèvre, M., 2009. Mountain building and
1136 exhumation processes through time: inferences from nature and models. *Terra Nova* 21, 188–194.
1137
- 1138 Gerdes, A. and Zeh, A., 2006. Combined U-Pb and Hf isotope LA-(MC)ICP-MS analyses of detrital
1139 zircons: Comparison with SHRIMP and new constraints for the provenance and age of an
1140 Armorican metasediment in Central Germany. *Earth and Pl. Sci. Letters* 249, 47-61.
1141
- 1142 Gerdes, A. and Zeh, A., 2009. Zircon formation versus zircon alteration: new insights from combined U-
1143 Pb and Lu-Hf in-situ LA-ICP-MS analyses, and consequences for the interpretation of Archaean
1144 zircon from the Central Zone of the Limpopo Belt. *Chem. Geol.* 261, 230-243.
1145
- 1146 Good, N. and M.J. De Wit, 1997. The Thabazimbi-Murchison Lineament of the Kaapvaal craton,
1147 South Africa : 2700 Ma of episodic deformation. *Journal of the Geological Society* 154, 1, 93-97.
1148
- 1149 Grambling, J.A., 1986. Crustal thickening during Proterozoic metamorphism and deformation in
1150 New Mexico. *Geology* 14, 149–152.
1151
- 1152 Griffin, W.L., O'Reilly, S.Y., Ryan, C.G., Gaul, O., Ionov, D., 1998. Secular variation in the
1153 composition of the subcontinental lithospheric mantle. In: Braun, J. et al. (eds). *Structure
1154 and Evolution of the Australian Continent*, Geodynamics Series, 26, American Geophysical
1155 Union, 1–25.
1156
- 1157 Henderson, D.R., Long, L.E. and Barton, J.M., 2000. Isotopic ages and chemical and isotopic
1158 compositions of the Archaean Turfloop Batholith, Pietersburg granite-greenstone terrane, Kaapvaal
1159 Craton, South Africa. *S. Afr. J. Geol.*, 103(1): 38-46.
1160

- 1161 Hurai, V., Paquette, J.-L., Huraiová, M., Konečný, P., 2010. U-Th-Pb geochronology of zircon and
1162 monazite from syenite and pincinite xenoliths in Pliocene alkali basalts of the intra-
1163 Carpathian back-arc basin. *J. Volcanol. Geotherm. Res.*, 198, 275-287.
- 1164
- 1165 Holland, T., Powell, R., 1996. Thermodynamics of order-disorder in minerals. 2. Symmetric formalism
1166 applied to solid solutions. *Am. Min.* **81**, 1425-37.
- 1167
- 1168 Holland, T.J.B. and Powell, R., 1998. An internally consistent thermodynamic data set for phases of
1169 petrological interest. *J. Metamorph. Geol.* **16**, 309-43
- 1170
- 1171 Holland, T., Baker, J., Powell, R. 1998. Mixing properties and activity-composition relationships of
1172 chlorites in the system MgO-FeO-Al₂O₃-SiO₂-H₂O. *European Journal of Mineralogy* **10**, 395
1173 406.
- 1174
- 1175 Holland, T., Powell, R., 2001. Calculation of phase relations involving haplogranitic melts using an
1176 internally consistent thermodynamic dataset. *J. Petrol.* **42**, 673-83.
- 1177
- 1178 Jaguin, J., Gapais, D., Poujol, M., Boulvais, P. et Moyen, J.F. (in press). The Murchison Greenstone Belt
1179 (South Africa) : a general tectonic framework. *S.Afr.J.Geol.*, 115, 1, 65-76.
- 1180
- 1181 Jackson, S.E., Pearson, N.J., Griffin, W.L., Belousova, E.A., 2004. The application of laser ablation-
1182 inductively coupled plasma-mass spectrometry to in situ U-Pb zircon geochronology. *Chem.*
1183 *Geol.*, 211, 47-69.
- 1184
- 1185 Kamo, S.L., Davis, D.W., 1994. Reassessment of Archaean crustal development in the Barberton
1186 Mountain Land, South Africa, based on U-Pb dating. *Tectonics* 13 (1), 167-192.

1187
1188 Kisters, A.F.M., Stevens, G., Dziggel, A., Armstrong, R.A., 2003. Extensional detachment faulting
1189 and core-complex formation in the southern Barberton granite-greenstone terrain, South
1190 Africa: evidence for a 3.2 Ga orogenic collapse. *Precambrian Res.* 127, 355–378.

1191
1192 Komiya, T., Maruyama, S., Masuda, T., Nobda, S., Hayashi, M. & Okamoto, K. 1999. Plate tectonics at
1193 3.8–3.7 Ga: Field evidence from the Isua Accretionary Complex, southern West Greenland. *Journal of*
1194 *Geology*, 107, 515–554.

1195
1196 Komiya, T., Hayashi, M., Maruyama, S. and Yurimoto, H., 2002. Intermediate-P/T type Archaean
1197 metamorphism of the Isua supracrustal belt: Implications for secular change of geothermal
1198 gradients at subduction zones and for Archaean plate tectonics. *American Journal of Science*, 302,
1199 806–826.

1200 Kröner, A., Byerly, G.R., Lowe, D.R., 1991. Chronology of early Archean granite–greenstone evolution
1201 in the Barberton Mountain Land, South Africa, based on precise dating by single grain zircon
1202 evaporation. *Earth Planet. Sci. Lett.* 103, 41–54.

1203
1204 Kröner, A., Hegner, E., Byerly, G.R., Lowe, D.R., 1992. Possible terrane identification in the early
1205 Archaean Barberton greenstone belt, South Africa, using single zircon geochronology. *EOS*
1206 *Trans. AGU, Fall Meeting Suppl.* 73 (43), 616.

1207
1208 Kröner, A., Tegtmeier, A., 1994. Gneiss–greenstone relationships in the Ancient Gneiss Complex of
1209 southwestern Swaziland, southern Africa, and implications for early crustal evolution.
1210 *Precambrian Res.* 67, 109–139.

1211
1212 Kröner, A., Hegner, E., Wendt, J.I., Byerly, G.R., 1996. The oldest part of the Barberton granitoid–

- 1213 greenstone terrain, South Africa: evidence for crust formation at 3.5 and 3.7 Ga. *Precambrian Res.*
1214 78, 105–124.
- 1215
- 1216 Kröner, A., Jaeckel, P., Brandl, G., 2000. Single zircon ages for felsic to intermediate rocks from the
1217 Pietersburg and Giyani greenstone belts and bordering granitoid orthogneisses, northern Kaapvaal
1218 Craton, South Africa. *J. Afr. Earth Sci.* 30 (4), 773– 793.
- 1219
- 1220 Kusky, T. M., 1991. Structural development of an Archean orogen, western Point Lake, Northwest
1221 Territories. *Tectonics*, 10, 4, p. 820-841.
- 1222
- 1223 Kusky, T.M., Vearncombe, J.R., 1997. Structural aspects. In: de Wit, M., Ashwal, L.D. (Eds.),
1224 Greenstone Belts. *Oxford Monogr. Geol. Geophys.* 35, 91–124.
- 1225
- 1226 Kusky, T. M. and Polat, A. 1999. Growth of granite–greenstone terranes at convergent margins, and
1227 stabilization of Archean cratons. *Tectonophysics* 305, 43–73
- 1228
- 1229 Kusky, T.M., Li, Jianghai, and Tucker, R.T., 2001. The Archean Dongwanzi ophiolite complex, North
1230 China Craton: 2.505 Billion Year Old Oceanic Crust and Mantle, *Science*, 292, 1142-1145.
- 1231
- 1232 Ludwig, K.R., 1998. On the Treatment of Concordant Uranium-Lead Ages. *GeCA*, 62, 4, 665-676.
- 1233
- 1234 Ludwig, K.R., 2001. *Isoplot/Ex*, rev. 2.49: a geochronological toolkit for Microsoft Excel. Berkeley
1235 Geochronology Center, Spec. Publ. 1a, 55 p.
- 1236
- 1237 Marmo, B.A., Clarke, G.L., Powell, R., 2002. Fractionation of bulk rock composition due to
1238 porphyroblast growth : effects on eclogite facies mineral equilibria, Pam Peninsula, New

Caledonia. *J. Metamorph. Geol.*, 20, 151-165.

Millonig, L., Zeh, A., Gerdes, A. & Klemd, R. (2008). Neoproterozoic high-grade metamorphism in the Central Zone of the Limpopo Belt (South Africa): Combined petrological and geochronological evidence from the Bulai pluton. *Lithos*, **103**, 333-351.

Millonig, L., Zeh, A., Gerdes, A., Klemd, R., Barton, J.M., 2010. Decompressional Heating of the Mahalapye Complex (Limpopo Belt, Botswana): a Response to Palaeoproterozoic Magmatic Underplating ? *J. Petrol.* 51, 3, 703-729.

Mints, M. V., Belousova, E. A., Konilov, A. N., Natapov, L. N., Shchipansky, A. A., Griffin, W. L., O'Reilly, S. Y., Dokukina, K. A., Kaulina, T. V., 2010. Mesoarchean subduction processes: 2.87 Ga eclogites from the Kola Peninsula, Russia. *Geology* 38, 739-742.

Miyashiro, A., 1961. Evolution of metamorphic belts. *J. Petrol.* 2, 277-311.

Moyen, J.F., Stevens, G., Kisters, A., 2006. Record of mid-Archean subduction from metamorphism in the Barberton Terrain, South Africa. *Nature* 442, 559-562

Newton, R.C., Charlu, T.V., Kleppa, O.J., 1980. Thermochemistry of the high structural state plagioclases. *GeCA* **44**, 933-41.

Park, R.G., 1982. Archean tectonics. *Geol. Rundsch.* 71, 22-37.

Percival, J.A., Fountain, D.M., Salisbury, M.H., 1992. Exposed crustal cross sections as windows on the

- 1265 lower crust. In: Fountain, D.M., Arculus, R.J., Kay, R.W. (Eds.), Continental Lower Crust. Elsevier,
1266 Amsterdam, 317–362.
- 1267
- 1268 Percival, J., 1994. Archean high-grade metamorphism. In: Condie, K.C. (Ed.), Archean crustal evolution.
1269 Developments in Precambrian Geology 1 1, Elsevier, 357-410..
- 1270
- 1271 Platt, J.P, and Visser, R.L.M., 1980. Extensional structures in anisotropic rocks. *J. Struct. Geol.* 2, 397-
1272 410.
- 1273
- 1274 Pujol, M., Robb, L.J., Respaut, J.P., Anhaeusser, C.R., 1996. 3.07–2.97 Ga greenstone belt formation in
1275 the northeastern Kaapvaal Craton: implications for the origin of the Witwatersrand Basin. *Econ. Geol.* 91
1276 (8), 1455–1461.
- 1277
- 1278 Pujol, M., Respaut, J.P., Robb, L.J. and Anhaeusser, C.R., 1997. New U-Pb and Pb-Pb data on the
1279 Murchison greenstone belt, South Africa and their implications for the origin of the
1280 Witwatersrand basin. 319, EGRU, Johannesburg.
- 1281
- 1282 Pujol, M. and Robb, L.J., 1999. New U-Pb zircon ages on gneisses and pegmatite from South of
1283 the Murchison greenstone belt, South Africa. *S. Afr. J. Geol.*, 102(2): 93- 97.
- 1284
- 1285
- 1286 Pujol, M., 2001. U–Pb isotopic evidence for episodic granitoid emplacement in the Murchison
1287 greenstone belt, South Africa. *J. Afr. Earth Sci.* 33, 155–163.
- 1288
- 1289 Powell R., Holland T. J. B. and Worley B., 1998. Calculating phase diagrams involving solid solutions via
1290 non-linear equations, with examples using THERMOCALC. *J. Metamorph. Geol.* 16, 577-588.

- 1291
- 1292 Reno, B.L., Brown, M., Kobayashi, O.T., Nakamura, E., Piccoli, P.M. and Trouw, R.A.J., 2009.
- 1293 Eclogite–high-pressure granulite metamorphism records early collision in West Gondwana: New
- 1294 data from the Southern Brasília Belt, Brazil. *J. Geol. Soc. Lond*, 166, 1013-1032.
- 1295
- 1296 Rey, P.F., and Houseman, G., 2006. Lithospheric scale gravitational flow: the impact of body forces on
- 1297 orogenic processes from Archaean to Phanerozoic, In: Buiter, S. J. H. and Schreurs, G.(eds). *Analogue*
- 1298 *and Numerical Modelling of Crustal Scale Processes*. *Geol. Soc. Lond. Spec. Publ.*, 253, 153–167.
- 1299
- 1300 Robb, L.J., Brandl, G., Anhaeusser, C.R., Poujol, M., 2006. Archaean Granitoid Intrusions, In: Johnson,
- 1301 M.R., Anhaeusser, C.R., Thomas, R.J., *The Geology of South Africa*, 2006.
- 1302
- 1303 Saha, L., Pant, N.C., Pati, J.K., Upadhyay, D., Berndt, J., Bhattacharya, A., Satynarayanan, M., 2011.
- 1304 Neoproterozoic high-pressure margarite–phengitic muscovite–chlorite corona mantled corundum in
- 1305 quartz-free high-Mg, Al phlogopite–chlorite schists from the Bundelkhand craton, north central
- 1306 India. *Contrib. Mineral. Petrol.* 161, 511–530.
- 1307
- 1308 Schwartz-Schampera, U., Terblanche, H., Oberthür, T., 2010. Volcanic-hosted massive sulfide deposits
- 1309 in the Murchison greenstone belt, South Africa. *Mineralium Deposita* 45, 2, 113-145.
- 1310
- 1311 Sizova, E., Gerya, T., Brown, M., Perchuk, L.L., 2010. Subduction styles in the Precambrian: insight
- 1312 from numerical experiments. *Lithos* 116, 3-4, 209-22.
- 1313
- 1314 Smith, D.C., 1984. Coesite in clinopyroxene in the Caledonides and its implications for geodynamics.
- 1315 *Nature* 310, 641–644.
- 1316

1317 South African Committee for Stratigraphy, 1980. Chapter 2.3: The Murchison Sequence, In: 559 C.L.E. Hart
1318 (Editor), Stratigraphy of South Africa, part 1: Lithostratigraphy of the 560 Republic of South Africa, South
1319 West Africa/Namibia and the Republics of 561 Bophuthatswana, Transkei and Venda. South Africa Geological
1320 Survey Handbook, 45-562 52.

1321
1322 Stacey, J.S and Kramers, J.D., 1975. Approximation of terrestrial lead isotope evolution by a two-stage
1323 model. Earth Planet. Sci. Lett. 26, 2, 207-221

1324
1325
1326 Stüwe, K., 1997. Effective bulk composition change due to cooling: a model predicting complexities in
1327 retrograde reaction textures. Contrib. Mineral. Petrol. 129, 43–52.

1328
1329 Tajcmanová, L., Connolly, J.A.D., Cesare, B., 2009. A thermodynamic model for titanium and ferric
1330 iron solution in biotite. J. Metamorph. Geol. **27**, 153-64.

1331
1332 Van Kranendonk, M.J., Hickman, A.H., Smithies, R.H., Nelson, D.N., Pike, G., 2002. Geology and
1333 tectonic evolution of the Archaean North Pilbara terrain, Pilbara Craton, Western Australia. Econ. Geol.
1334 97, 695–732.

1335
1336 Vearncombe, J.R., Barton, J.M. and Walsh, K.L. (1987). The Rooiwater Complex and associated rocks,
1337 Murchison granitoid-greenstone terrane, Kaapvaal Craton. S. Afr. J. Geol., 90, 361-377.

1338
1339 Vearncombe, J. R., Cheshire, P. E., De Beer, J. H., Killick, A. M., Mallinson, W. S., McCourt, S., et al.,
1340 1988a. Structures related to the Antimony line, Murchison schist belt, Kaapvaal craton, South Africa.
1341 Tectonophysics, 154 (3-4), 285-308.

- 1343 Vearncombe, J. R., 1988b. Structure and metamorphism of the Archean Murchison Belt, Kaapvaal
1344 Craton, South Africa. *Tectonics*, 7(4), 761-774.
- 1345
- 1346 Vearncombe, J. R., Barton, J. M., Cheshire, P. E., De Beer, J. H., Stettler, E. H., and Brandl, G., 1992.
1347 Geology, geophysics and mineralization of the Murchison Schist Belt, Rooiwater Complex and
1348 surrounding granitoids, Memoir of the Geological Survey of South Africa, 81, 139p.
- 1349
- 1350 Viljoen, M.J, Van Vuuren, C.J.J., Pearton, P.N., Minnitt, R.C.A., Muff, R. and Cillier, P., 1978. The
1351 regional geological setting of mineralization in the Murchison Range with particular reference to
1352 antimony. In : Verwoerd, W.J. (Ed.), *Mineralization in Metamorphic Terranes*. Spec. Publ. Geol. Soc.
1353 S. Afr., 1, 661-668.
- 1354
- 1355 Volodichev, O., Slabunov, A., Bibikova, E., Konilov, A., Kuzenko, T., 2004. Archean eclogites in the
1356 Belomorian mobile belt, Baltic Shield. *Petrology*, 12, 540–560.
- 1357
- 1358 Waldbaum, D.R., Thompson, J.B., 1968. Mixing Properties Of Sanidine Crystalline Solutions .2.
1359 Calculations Based On Volume Data. *Am. Min.* **53**, 2000-?
- 1360
- 1361 Watts, A.B. and Burov, E.B., 2003. Lithospheric strength and its relationship to the elastic and
1362 seismogenic layer thickness. *Earth Planet. Sci. Lett.* 213, 113-131.
- 1363
- 1364 White, R.W., Powell, R., Holland, T.J.B., Worley, B.A. 2000b. The effect of TiO₂ and Fe₂ O₃ on
1365 metapelitic assemblages at greenschist and amphibolite facies conditions: mineral equilibria
1366 calculations in the system K₂ O-FeO-MgO-Al₂ O₃-SiO₂ -H₂ O-TiO₂ Fe₂ O₃. *J. Metamorph. Geol.*
1367 **18**:497-511.
- 1368

- 1369 Zeh, A., 2001. Inference of a detailed P-T path from P-T pseudosections using metapelitic rocks of
1370 variable composition from a single outcrop, Shackleton Range, Antarctica. *J. Metamorph.*
1371 *Geol.*, 19, 329-350.
- 1372
- 1373 Zeh, A., Klemd, R., Buhlmann, S., Barton J.M., 2004. Pro- and retrograde P-T evolution of granulites of
1374 the Beit Bridge Complex (Limpopo Belt, South Africa): constraints from quantitative phase diagrams
1375 and geotectonic implications. *J. Metamorph. Geol.*, 22, 79-95.
- 1376
- 1377
- 1378 Zeh, A., 2006. Calculation of garnet fractionation in natural metamorphic rocks, with application to a flat-
1379 top, Y-rich garnet population from the Ruhla Crystalline Complex, Central Germany. *J. Petrol.*, 47,
1380 2335-2356.
- 1381
- 1382 Zeh, A., Gerdes, A. and Barton, J.M., 2009. Archean Accretion and Crustal Evolution of the Kalahari
1383 Craton - the Zircon Age and Hf Isotope Record of Granitic Rocks from Barberton/Swaziland to the
1384 Francistown Arc. *J. Petrol.*, 50, 933-966.
- 1385
- 1386